

Coupling Finite Elements and Auxiliary Sources for Electromagnetic Wave Propagation

D. Casati and R. Hiptmair and J. Smajic

Research Report No. 2019-62

December 2019

Latest revision: May 2020

Seminar für Angewandte Mathematik
Eidgenössische Technische Hochschule
CH-8092 Zürich
Switzerland

REPORT

Coupling Finite Elements and Auxiliary Sources for Electromagnetic Wave Propagation

Daniele Casati^{*1} | Ralf Hiptmair¹ | Jasmin Smajic²

¹Seminar for Applied Mathematics,
ETH Zurich, Zurich, Switzerland

²Institute for Energy Technology,
Hochschule für Technik Rapperswil,
Zurich, Switzerland

Correspondence

*Daniele Casati, Email:
daniele.casati@sam.math.ethz.ch

Present Address

Seminar for Applied Mathematics,
ETH Zurich, Zurich, Switzerland

Summary

We propose four approaches to solve time-harmonic Maxwell's equations in \mathbb{R}^3 through the Finite Element Method (FEM) in a bounded region encompassing parameter inhomogeneities, coupled with the Multiple Multipole Program (MMP) in the unbounded complement.

MMP belongs to the class of methods of auxiliary sources and of Trefftz methods, as it employs point sources that spawn exact solutions of the homogeneous equations. Each of these sources is anchored at a point that, if singular, is placed outside the respective domain of approximation.

In the MMP domain we assume that material parameters are piecewise constant, which induces a partition into one unbounded subdomain and other bounded, but possibly very large, subdomains, each requiring its own MMP trial space. Hence, in addition to the transmission conditions between the FEM and MMP domains, one also has to impose transmission conditions connecting the MMP subdomains.

Coupling approaches arise from seeking stationary points of Lagrangian functionals that both enforce the variational form of the equations in the FEM domain and match the different trial functions across subdomain interfaces. We discuss the following approaches:

1. Least-squares-based coupling using techniques from PDE-constrained optimization.
2. Discontinuous Galerkin coupling between the meshed FEM domain and the single-entity MMP subdomains.
3. Multi-field variational formulation in the spirit of mortar finite element methods.
4. Coupling through the Dirichlet-to-Neumann operator.

We compare these approaches in a series of numerical experiments with different geometries and material parameters, including examples that exhibit triple-point singularities and infinite layered media.

KEYWORDS:

finite element method, multiple multipole program, method of auxiliary sources, Trefftz method, computational electromagnetics

1 | INTRODUCTION

We devise a hybrid method based on domain decomposition by proposing four ways to couple the *Finite Element Method* (FEM) and a *Trefftz method* (Section 2). Specifically, we make use of the Trefftz method known as *Multiple Multipole Program* (MMP) – see Section 2.1.

Trefftz methods employ exact solutions of the homogeneous PDE as basis functions; hence, they can handle unbounded domains and, compared to standard FEM, the FEM–Trefftz coupling will not need to artificially truncate the computational domain.

At the same time, Trefftz methods can only be applied to domains with constant material parameters. Here we consider them *piecewise constant* in the Trefftz domain of approximation, which induces a partition: we assume that only one subdomain is unbounded, but the other bounded subdomains can still be very large. By using a Trefftz method in this whole region, the meshed domain required by FEM can be made minimal¹.

Several approaches to couple FEM and a Trefftz method for the Poisson's equation in both 2D and 3D have been discussed by the authors from the perspective of numerical analysis in [?]. Existence, uniqueness, and stability of all coupling approaches is formally proven in that work, which only deals with scalar unknown functions. We offered numerical evidence for the feasibility of the coupling for Maxwell's equations (vector unknown functions) in [?], which illustrate numerical convergence results for the magnetostatic and eddy-current equations, respectively.

The work [?] generalizes one of the coupling approaches, the *Dirichlet-to-Neumann-based coupling* (DtN-based coupling, Section 3.3.2), to any numerical method based on volume meshes. The particular case of the coupling with the *cell method*, a technique based on both a primal and a dual volume mesh [?], is illustrated theoretically and through numerical experiments performed with iterative solvers applied to the Schur complement of the coupling systems (Trefftz degrees of freedom are eliminated).

Finally, [?] assumes that material parameters are piecewise constant in the Trefftz domain, similarly to what is done in this work, to solve the 2D Helmholtz equation. The approaches we propose here to realize the coupling between FEM and more than one Trefftz domain have been described there for the first time.

To the best of our knowledge, apart from these papers, little research has been devoted to the investigation of strategies combining Trefftz methods with conventional finite element methods.

As references for this line of research, we cite [? ? ?]: in particular, the coupling proposed in [? , p. 672, Section III] is the same as the DtN-based coupling of Section 3.3.2. It is also worth mentioning the *infinite element method* [?], primarily used for exterior Helmholtz problems, which employs standard FEM in a bounded domain and *infinite elements* [? , p. 100, (3.19)], akin to *multipole expansions* (Section 2.1), in the unbounded exterior.

The novelty of the present work lies in using FEM with more than one Trefftz domain to solve nontrivial problems involving time-harmonic Maxwell's equations, while [?] is confined to 2D Helmholtz. This work also includes a numerical example involving *infinite layered media* [?] (Section 4.2.2).

1.1 | Boundary Value Problem

We consider the following second-order vector boundary value problem:

$$\begin{cases} \nabla \times [\mathbf{M}_\mu^{-1}(\mathbf{x}) \nabla \times \mathbf{u}] - \omega^2 \mathbf{M}_\epsilon(\mathbf{x}) \mathbf{u} + \nabla \phi = \mathbf{j} & \text{in } \mathbb{R}^3, \\ \nabla \cdot \mathbf{u} = 0 \end{cases} \quad (1a)$$

$$\nabla \times \mathbf{u} \times \mathbf{x} - ik\|\mathbf{x}\|\mathbf{u} = \mathbf{0} \quad \text{for } \|\mathbf{x}\| \rightarrow \infty \text{ uniformly}, \quad (1b)$$

which models time-harmonic Maxwell's equations (frequency-domain electromagnetic wave propagation) expressed in terms of a magnetic vector potential subject to the Coulomb gauge.

- $\mathbf{u}: \mathbb{R}^3 \rightarrow \mathbb{C}^3$ represents the magnetic vector potential. The first line in (1a) comprises Maxwell's equations², the second the Coulomb gauge.
- $\phi: \mathbb{R}^3 \rightarrow \mathbb{C}$ represents the electric scalar potential, which also acts as a Lagrange multiplier to impose the Coulomb gauge. ϕ must be subject to a further constrain such that it is uniquely defined by (1a). In the scope of this work, we set $\int_{\mathbb{R}^3} \phi \, d\mathbf{x} = 0$.

⁰**Abbreviations.** FEM: Finite Element Method. MMP: Multiple Multipole Program. PDE: Partial Differential Equation. TPS: Triple-Point Singularity. DtN: Dirichlet-to-Neumann. DG: Discontinuous Galerkin. DoF: Degree of Freedom. BEM: Boundary Element Method. Subscript f in formulas: FEM. Subscript m in formulas: MMP. Superscript n in formulas: discrete.

¹In particular, the mesh can be so small that it only surrounds points where the field is singular, like *Triple-Point Singularities* (TPS), which emerge at the junction of three different materials [?] (Section 4.2).

²The first equation of (1a) can be obtained by substituting $\mathbf{B} = \nabla \times \mathbf{u}$, with $\mathbf{B}: \mathbb{R}^3 \rightarrow \mathbb{C}^3$ magnetic flux density, and $\mathbf{E} = -\nabla \phi + i\omega \mathbf{u}$, with $\mathbf{E}: \mathbb{R}^3 \rightarrow \mathbb{C}^3$ electric field, into Ampère's law [? , p. 4, (1.4c)].

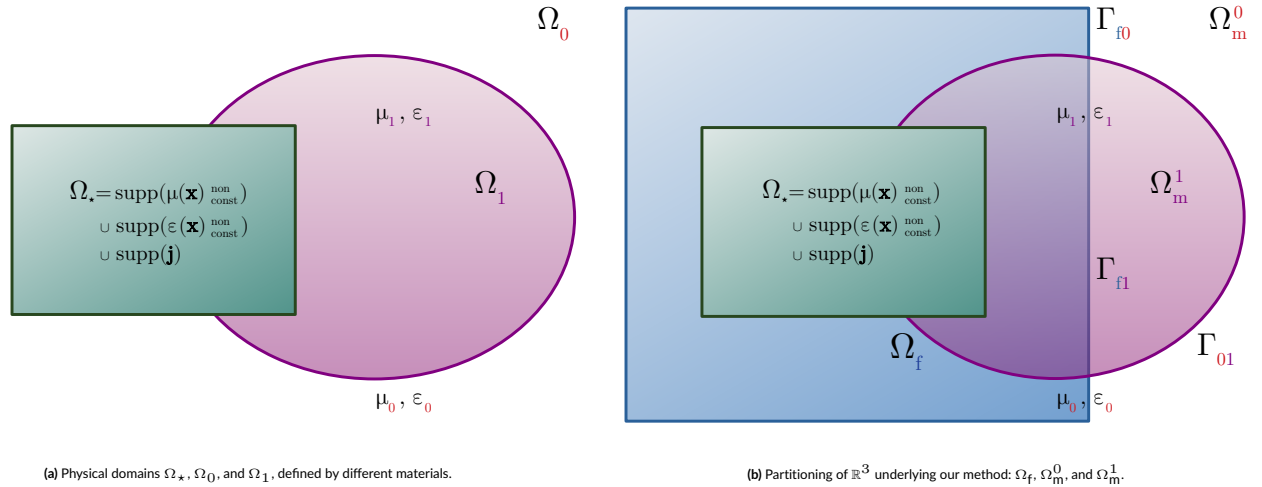


FIGURE 1 Physical domains (Figure 1a) do not necessarily correspond to computational domains (Figure 1b): Γ_{f0} , Γ_{f1} can be artificial interfaces. Different colors in the figure represent regions with different parameters μ , ϵ .

- $\mathbf{M}_\mu, \mathbf{M}_\epsilon : \mathbb{R}^3 \rightarrow \mathbb{C}^{3,3}$ are symmetric, bounded, uniformly positive-definite matrices that correspond to an inhomogeneous, anisotropic permeability and permittivity, respectively. We assume that both $\mathbf{M}_\mu(\mathbf{x}) = \mu \mathbf{I}$ and $\mathbf{M}_\epsilon(\mathbf{x}) = \epsilon \mathbf{I} \quad \forall \mathbf{x} \in \mathbb{R}^3 \setminus \Omega_*$, given a bounded domain $\Omega_* \subset \mathbb{R}^3$, and μ, ϵ are piecewise constant in $\mathbb{R}^3 \setminus \Omega_*$.
- $\omega \in \mathbb{R}$ is the angular frequency, while $k := \omega \sqrt{\mu \epsilon}$ the piecewise-constant wavenumber in $\mathbb{R}^3 \setminus \Omega_*$. It is implicitly assumed that $k \neq 0$; otherwise, if, e.g., $\omega = 0$, we would be in a magnetostatic regime. This case is discussed in [?].
- $\mathbf{j} : \mathbb{R}^3 \rightarrow \mathbb{R}^3$, with $\nabla \cdot \mathbf{j} = 0$, represents the stationary current that generates the electromagnetic field. \mathbf{j} has compact support in Ω_* .
- (1b) is the *Silver-Müller radiation condition*; please refer to [?, p. 195, Definition 6.6].

1.2 | Domain Decomposition

Piecewise-constant μ, ϵ in $\mathbb{R}^3 \setminus \Omega_*$ induce a natural partition of $\mathbb{R}^3 \setminus \Omega_*$ into $m + 1$ subdomains Ω_i , $i = 0, \dots, m$, such that the pair $(\mu, \epsilon) \in \mathbb{C}^2$ (and therefore the wavenumber k) is constant in each Ω_i . We denote the constant wavenumber for each subdomain with k_i , $i = 0, \dots, m$, and assume that there is only one unbounded domain in this partition, which we refer to as Ω_0 .

To simplify the exposition and without loss of generality, from now on we assume that $m = 1$, i.e. that $\Omega_0 \cup \Omega_1 = \mathbb{R}^3 \setminus \Omega_*$, with constant $k_0 \in \mathbb{C}$ in the unbounded domain Ω_0 and constant $k_1 \in \mathbb{C}$ in the bounded Ω_1 . Generalization to $m > 1$ is immediate.

However, instead of considering the physical domains $\Omega_*, \Omega_0, \Omega_1$ (see Figure 1a), we take a different partition for computations (see Figure 1b):

$$\mathbb{R}^3 = \Omega_f \cup \Omega_m^0 \cup \Omega_m^1 \cup \Gamma_{f0} \cup \Gamma_{f1} \cup \Gamma_{01}, \quad (2)$$

with $\Gamma_{f0} := \partial\Omega_f \cap \partial\Omega_m^0$, $\Gamma_{f1} := \partial\Omega_f \cap \partial\Omega_m^1$, $\Gamma_{01} := \partial\Omega_m^0 \cap \partial\Omega_m^1$ and $\Omega_f \cap \Omega_m^0 = \emptyset$, $\Omega_f \cap \Omega_m^1 = \emptyset$, $\Omega_m^0 \cap \Omega_m^1 = \emptyset$. We also define $\Omega_m := \Omega_m^0 \cup \Omega_m^1$ and $\Gamma := \Gamma_{f0} \cup \Gamma_{f1} \cup \Gamma_{01}$.

We demand $\Omega_* \subseteq \Omega_f$, but not necessarily $\Omega_* = \Omega_f$. If $\Omega_* \neq \Omega_f$, $\Gamma_{f0} \cup \Gamma_{f1} = \partial\Omega_f$ is an *artificial interface*. Note that Ω_f can be composed of disjoint regions.

We also demand that Ω_m^0, Ω_m^1 include different values of the material parameters of (1a): $\Omega_m^i \subseteq \Omega_i$, $i = 0, 1$, i.e. constant wavenumbers k_0, k_1 for Ω_m^0, Ω_m^1 .

We call Ω_f , a bounded Lipschitz domain, the *FEM domain*, whereas Ω_m^0 is the unbounded and Ω_m^1 the bounded *Trefftz domain*. The terminology indicates the type of approximation of the unknown to be employed in each domain. Coupling between the FEM and Trefftz domains is done across the (artificial) interfaces Γ_{fi} , $i = 0, 1$, while coupling between the two Trefftz domains occurs across the physical interface Γ_{01} .

Given these computational domains and using $_f$ and $_m$ as subscripts for FEM and Trefftz methods, respectively, we can decompose \mathbf{u} , ϕ as

$$\mathbf{u}_f := \mathbf{u}|_{\Omega_f} \in \mathbf{H}(\mathbf{curl}, \Omega_f), \quad \mathbf{u}_m^0 := \mathbf{u}|_{\Omega_m^0} \in \mathbf{H}_{\text{loc}}(\mathbf{curl}, \Omega_m^0), \quad \mathbf{u}_m^1 := \mathbf{u}|_{\Omega_m^1} \in \mathbf{H}(\mathbf{curl}, \Omega_m^1), \quad (3a)$$

$$\phi_f := \phi|_{\Omega_f} \in H_*^1(\Omega_f), \quad \phi_m^0 := \phi|_{\Omega_m^0} \in H_{*,\text{loc}}^1(\Omega_m^0), \quad \phi_m^1 := \phi|_{\Omega_m^1} \in H_*^1(\Omega_m^1), \quad (3b)$$

with $H_*^1(\Omega_f) := \left\{ \varphi \in H^1(\Omega_f) : \int_{\Omega_f} \varphi \, dx = 0 \right\}$. The subscript “loc” indicates that functions belong to the reported space after multiplication with a compactly-supported smooth function [?, p. 230].

1.3 | Discretization

By testing the integral form of (1a) on Ω_f with suitable functions and integrating by parts, we obtain

Seek $\mathbf{u}_f \in \mathbf{H}(\mathbf{curl}, \Omega_f)$, $\phi_f \in H_*^1(\Omega_f)$:

$$\begin{cases} \int_{\Omega_f} \left[\left(\mathbf{M}_\mu^{-1} \nabla \times \mathbf{u}_f \right) \cdot (\nabla \times \mathbf{v}_f) - \omega^2 (\mathbf{M}_\epsilon \mathbf{u}_f) \cdot \mathbf{v}_f \right] dx + \sum_{i=0,1} \int_{\Gamma_{fi}} \gamma \mathbf{u}_f^i \cdot \mathbf{v}_f \, dS + \int_{\Omega_f} \nabla \phi_f \cdot \mathbf{v}_f \, dx = \int_{\Omega_f} \mathbf{j} \cdot \mathbf{v}_f \, dx & \forall \mathbf{v}_f \in \mathbf{H}(\mathbf{curl}, \Omega_f), \\ \int_{\Omega_f} \mathbf{u}_f \cdot \nabla \psi_f \, dx - \sum_{i=0,1} \int_{\Gamma_{fi}} (\mathbf{n} \cdot \mathbf{u}_f^i) \psi_f \, dS = 0 & \forall \psi_f \in H_*^1(\Omega_f), \end{cases} \quad (4)$$

given the *magnetic trace* γ [?, p. 59, (3.51)]

$$\gamma: \begin{cases} \mathbf{H}_{\text{loc}}(\mathbf{curl} \, \mathbf{curl}, \Omega_\square) \rightarrow \tilde{\mathbf{H}}^{-\frac{1}{2}}(\text{div}_{\Gamma_\square}, \Gamma_\square), \\ \mathbf{v} \mapsto \mathbf{n} \times \left(\mathbf{M}_\mu^{-1} \nabla \times \mathbf{v} \right). \end{cases} \quad (5)$$

We define the terms appearing in (5):

- $\Omega_\square \in \{ \Omega_f, \Omega_m^0, \Omega_m^1 \}$ and $\Gamma_\square \in \{ \Gamma_{f0}, \Gamma_{f1}, \Gamma_{01} \}$.
- $\mathbf{H}_{\text{loc}}(\mathbf{curl} \, \mathbf{curl}, \Omega_\square)$ is the space of functions $\mathbf{v} \in \mathbf{H}_{\text{loc}}(\mathbf{curl}, \Omega_\square)$ for which $\nabla \times (\nabla \times \mathbf{v}) \in \mathbf{L}_{\text{loc}}^2(\Omega_\square) := [L_{\text{loc}}^2(\Omega)]^3$.
- $\tilde{\mathbf{H}}^{-\frac{1}{2}}(\text{div}_{\Gamma_\square}, \Gamma_\square)$ [?, p. 59] is the dual space of $\mathbf{H}^{-\frac{1}{2}}(\mathbf{curl}_{\Gamma_\square}, \Gamma_\square)$ [?, p. 59, (3.53)]. The tilde of $\tilde{\mathbf{H}}^{-\frac{1}{2}}(\text{div}_{\Gamma_\square}, \Gamma_\square)$ takes into account that Γ_\square is generally an open interface [?, p. 59, (2.90)].
- \mathbf{n} is the normal vector on Γ_\square .

We use standard finite element spaces to discretize (4) in $\Omega_f \supseteq \Omega_*$, where $\mathbf{M}_\mu, \mathbf{M}_\epsilon$ may vary in space. These discrete spaces are built on tetrahedral meshes \mathcal{M}_f on Ω_f . More specifically, we discretize $\mathbf{u}_f \in \mathbf{H}(\mathbf{curl}, \Omega_f)$ with the lowest-order $\mathbf{H}(\mathbf{curl}, \Omega_f)$ -conforming edge elements of the first family due to Nédélec [?, p. 126, Section 5.5], i.e.

$$V^n(\mathcal{M}_f) := \mathcal{R}^1(\mathcal{M}_f) := \left\{ v^n \in \mathbf{H}_0(\mathbf{curl}, \Omega_f) : v^n|_K(\mathbf{x}) = \mathbf{a}_K + \mathbf{b}_K \times \mathbf{x}, \quad \mathbf{a}_K, \mathbf{b}_K \in \mathbb{R}^3, \mathbf{x} \in K \quad \forall K \in \mathcal{M}_f \right\}, \quad (6a)$$

and $\phi_f \in H_*^1(\Omega_f)$ with piecewise-linear Lagrangian finite elements [?, p. 143, Section 5.6], i.e.

$$V^n(\mathcal{M}_f) := \mathcal{S}_1^0(\mathcal{M}_f) := \left\{ v^n \in C^0(\Omega_f) : v^n|_K(\mathbf{x}) = a_K + \mathbf{b}_K \cdot \mathbf{x}, \quad a_K \in \mathbb{R}, \mathbf{b}_K \in \mathbb{R}^3, \mathbf{x} \in K \quad \forall K \in \mathcal{M}_f \right\}. \quad (6b)$$

On each discrete function $\phi_f^n \in H_*^1(\Omega_f)$ discretized by $V^n(\mathcal{M}_f) \subset H^1(\Omega_f)$ we impose the condition $\int_{\Omega_f} \phi_f^n \, dx = 0$ by means of a scalar Lagrange multiplier.

However, in the partition of $\mathbb{R}^3 \setminus \Omega_f$, induced by piecewise-constant material parameters μ, ϵ and giving rise to the unbounded domain Ω_m^0 and the (possibly very large) domain Ω_m^1 (Figure 1a), we do not intend to employ mesh-based basis functions, as required by Ω_* . Indeed, given the computational domains Ω_m^0, Ω_m^1 introduced in Section 1.2, the weak solution $\mathbf{u}_m^0 \in \mathbf{H}_{\text{loc}}(\mathbf{curl}, \Omega_m^0)$ of (1) is sought in the continuous *Trefftz space*

$$\mathcal{T}(\Omega_m^0) := \left\{ \mathbf{v} \in \mathbf{H}_{\text{loc}}(\mathbf{curl}, \Omega_m^0) : \nabla \times (\nabla \times \mathbf{v}) - k_0^2 \mathbf{u} = \mathbf{0}, \quad k_0 \in \mathbb{C}, \quad \nabla \cdot \mathbf{v} = 0, \right. \\ \left. \mathbf{v} \text{ satisfies the radiation condition (1b)} \right\}, \quad (7a)$$

which is composed of exact solutions of (1) in Ω_m^0 . Correspondingly, $\mathbf{u}_m^1 \in \mathbf{H}(\mathbf{curl}, \Omega_m^1)$ is sought in

$$\mathcal{T}(\Omega_m^1) := \left\{ \mathbf{v} \in \mathbf{H}(\mathbf{curl}, \Omega_m^1) : \nabla \times (\nabla \times \mathbf{v}) - k_1^2 \mathbf{u} = \mathbf{0}, \quad k_1 \in \mathbb{C}, \quad \nabla \cdot \mathbf{v} = 0 \right\}. \quad (7b)$$

Trefftz methods seek to approximate the unknown in Ω_m^0, Ω_m^1 using finite-dimensional (discrete) subspaces of $\mathcal{T}(\Omega_m^0), \mathcal{T}(\Omega_m^1)$. While mesh-based methods like FEM suffer from the well-known *pollution effect* [?] with time-harmonic Maxwell's equations, $\mathcal{T}(\Omega_m^0), \mathcal{T}(\Omega_m^1)$ contain oscillating basis functions, which may achieve better approximation properties than the classical piecewise-polynomial spaces of FEM [?]. Specifically, our approach uses multipole expansions centered in points outside each $\Omega_i, i = 0, 1$, which is being approximated; see the next Section 2 for details.

2 | TREFFTZ METHODS

Trefftz methods rely on *Trefftz spaces* spanned by functions that are exact solutions of the PDE of interest, not necessarily independent from each other. Important choices of these *Trefftz basis functions* are

- *plane waves* and (*generalized*) *harmonic polynomials* [?],
- *fundamental solutions* with singularities outside the domain of Trefftz approximation [?], and
- fields spawned by point sources, also located outside the Trefftz domain (*method of auxiliary sources*³ [?]).

In spite of this diversity, all Trefftz methods share a desirable feature and a drawback. The former is the exponential convergence of their approximation error if the field is sufficiently smooth (see Section 2.2). The drawback is that, as exact solutions of a PDE are global functions and simple choices for a basis of $\mathcal{T}(\Omega_m^0)$, $\mathcal{T}(\Omega_m^1)$ may be affected by near-linear dependence, Trefftz basis functions typically lead to ill-conditioned dense matrices.

Thus, stability is an issue, even if mitigated by the few degrees of freedom of Trefftz methods, given their exponential convergence. Related is the need of heuristic rules to build the discrete Trefftz spaces when the unknown is difficult to model, e.g., when close to singularities: instability can have such a large impact that the numerical solution becomes useless.

The numerical examples of Section 4 show that coupling a Trefftz method with FEM can be a way to overcome this issue. There we use Trefftz spaces spanned by *multipoles* and refer to this discretization as the MMP approximation after the Trefftz method known as *Multiple Multipole Program*.

2.1 | Multiple Multipole Program

The concept of the Multiple Multipole Program was proposed by Ch. Hafner in his dissertation [?] and popularized by his free code `OpenMaxwell` [?] for 2D axisymmetric problems. Hafner's MMP is in turn based on the much older work of G. Mie and I. N. Vekua [? ?]. Essentially, the Mie-Vekua approach expands some scalar field in a 2D multiply-connected domain by a multipole expansion supplemented with generalized harmonic polynomials. Extending these ideas, MMP introduces more basis functions (*multipole multipoles*) than required according to Vekua's theory [?] to span the MMP Trefftz spaces (7).

Multipoles are potentials spawned by (anisotropic) point sources. For this reason, MMP belongs to the class of methods of auxiliary sources. These point sources are taken from the exact solutions of the homogeneous PDEs (1a) that can be subject to the decay condition (1b), depending on whether they are used to approximate the solution in Ω_m^0 .

A multipole can generally be written as $\mathbf{v}(\mathbf{x}) := f(r_{xc}) \mathbf{g}(\theta_{xc}, \varphi_{xc})$ in a spherical coordinate system in \mathbb{R}^3 ($r \in [0, \infty)$, $\theta \in [0, 2\pi)$, $\varphi \in [0, \pi]$) with respect to its center $\mathbf{c} \in \mathbb{R}^3$ ($\mathbf{x}, \mathbf{c} \in \mathbb{R}^3$ are position vectors in Cartesian coordinates). Here, $(r_{xc}, \theta_{xc}, \varphi_{xc})^\top$ are spherical coordinates of the vector $\mathbf{x}_c := \mathbf{x} - \mathbf{c}$.

The radial dependence $f(r_{xc})$ may induce a central singularity, $|f(r)| \rightarrow \infty$ for $r \rightarrow 0$, and, when needed, the desired decay condition at infinity. If they feature a singularity, multipoles are centered outside the domain in which they are used for approximation.

On the other hand, the spherical dependence \mathbf{g} is usually formulated in terms of vector spherical harmonics [? , p. 289]. The additional constraint of the Coulomb gauge in (1a) is taken into account by selecting a subset of vector spherical harmonics to express \mathbf{g} .

More specifically, the multipoles chosen for the numerical experiments of Section 4 have the forms

$$(r, \theta, \varphi) \mapsto \begin{cases} b_\ell(kr_{xc}) \Phi_{\ell m}(\theta_{xc}, \varphi_{xc}), \\ \ell(\ell+1) \frac{b_\ell(kr_{xc})}{kr_{xc}} \mathbf{Y}_{\ell m}(\theta_{xc}, \varphi_{xc}) + \left[b'_\ell(kr_{xc}) + \frac{b_\ell(kr_{xc})}{kr_{xc}} \right] \Psi_{\ell m}(\theta_{xc}, \varphi_{xc}), \\ \ell = 1, \dots, \infty, \quad m = -\ell, \dots, \ell, \end{cases} \quad (8)$$

given vector spherical harmonics defined as

$$\mathbf{Y}_{\ell m}(\theta, \varphi) := \mathbf{e}_r Y_{\ell m}(\theta, \varphi), \quad \mathbf{e}_r = (1, 0, 0)^\top, \quad (9a)$$

$$\Phi_{\ell m}(\theta, \varphi) := \mathbf{r} \times \nabla_{\text{sph}} Y_{\ell m}(\theta, \varphi), \quad \mathbf{r} = (r, 0, 0)^\top, \quad (9b)$$

$$\Psi_{\ell m}(\theta, \varphi) := r \nabla_{\text{sph}} Y_{\ell m}(\theta, \varphi), \quad (9c)$$

here with spherical components.

³A special method of auxiliary sources is the *Multiple Multipole Program*, which employs *multipole expansions* – see Section 2.1.

- b_ℓ is a spherical Hankel function of the first kind $h_\ell^{(1)}$ [?, p. 281] or a spherical Bessel function of the first kind j_ℓ [?, p. 279], depending on whether the Trefftz space is subject to the Silver-Müller radiation condition (1b).
- $k := \omega\sqrt{\mu\epsilon} \in \mathbb{C}$ is the piecewise-constant wavenumber: $k = k_i$ in Ω_m^i , $i = 0, 1$.
- ∇_{sph} denotes the gradient in spherical coordinates and $Y_{\ell m}(\theta, \varphi)$ the spherical harmonics [?, p. 250]. It can be shown that $\Phi_{\ell m}, \Psi_{\ell m}$ do not depend on r despite its presence in their definitions (9b) and (9c).

Each multipole from (8) is characterized by a location, i.e. its center \mathbf{c} , and parameters ℓ (degree) and m (subdegree). When we place several multipoles at a given location up to a certain order, which is the maximum degree of multipoles with that center, we use the term *multipole expansion*. Summing the number of terms of all multipole expansions used for approximation yields the total number of degrees of freedom of the discretized Trefftz space $\mathcal{T}^n(\Omega_m^i) \subset \mathcal{T}(\Omega_m^i)$ of (7), $i = 0, 1$.

2.2 | Approximation Error

For the Poisson's equation in an unbounded domain $\mathbb{R}^2 \setminus \Omega_*$, with Ω_* bounded domain, it can be proven that the approximation error in the H^1 -norm decreases exponentially with respect to the number of degrees of freedom of the corresponding MMP Trefftz space if the unknown possesses an analytic extension beyond the Trefftz domain [?, p. 3, Proposition 1]. The proof relies on the fact that (generalized) harmonic polynomials also achieve exponential convergence in H^i -seminorms, $i = 0, \dots, j$, $j \in \mathbb{N}_0$, when solving 2D Poisson in a bounded domain that satisfies certain assumptions [?, p. 61, Theorem 3.2.5].

A corresponding result for \mathbb{R}^3 remains elusive, even if [?, p. 261, Section 5.1] provides estimates for Trefftz approximations of functions with limited smoothness.

However, MMP without modifications cannot properly handle problems without an analytic extension, such as those with triple-point singularities (Section 4.2), and preserve its exponential behavior. There are two ways to cope with these situations:

1. Augmenting the Trefftz spaces with basis functions that capture the singularities [?]. However, explicit knowledge of the form of such singularities is required.
2. Coupling MMP with a method based on volume meshes, like FEM, and applying the latter to a locally-refined mesh that encompasses both the singularities and their immediate surrounding regions. By truncating the mesh at an auxiliary boundary that does not coincide with any physical discontinuity, MMP can be applied to a region where the field is sufficiently easy to approximate that heuristics on the placement of multipoles does not impact much on the quality of the solution. This is the approach followed by this work.

3 | COUPLING STRATEGIES

Relying on the formalism introduced in Sections 1.2 and 1.3, we can write the *transmission conditions* that the restrictions of the solution of (1) have to satisfy across Γ_{f_i} , $i = 0, 1$ [?, p. 107, Lemma 5.3]:

$$\mathbf{n} \times \mathbf{u}_f|_{\Gamma_{f_i}} = \mathbf{n} \times \mathbf{u}_m^i|_{\Gamma_{f_i}}, \quad (10a)$$

$$\boldsymbol{\gamma} \mathbf{u}_f|_{\Gamma_{f_i}} = \boldsymbol{\gamma} \mathbf{u}_m^i|_{\Gamma_{f_i}}, \quad (10b)$$

$$\mathbf{n} \cdot \mathbf{u}_f|_{\Gamma_{f_i}} = \mathbf{n} \cdot \mathbf{u}_m^i|_{\Gamma_{f_i}}. \quad (10c)$$

(10a) and (10b) stem from the first line of (1a), (10c) from the second line (Coulomb gauge).⁴ Analogous conditions also have to hold across Γ_{01} .

transmission conditions (10) on $\Gamma_{f_0}, \Gamma_{f_1}, \Gamma_{01}$ and the weak form (4) of (1a) in Ω_f are all the ingredients to obtain a FEM–Trefftz coupled solution of (1). By inserting (10b) and (10c) on $\Gamma_{f_0}, \Gamma_{f_1}$ into the boundary integrals of (4), we obtain

Seek $\mathbf{u}_f \in \mathbf{H}_\Gamma(\mathbf{curl}, \Omega_f)$, $\mathbf{u}_m^0 \in \mathcal{T}(\Omega_m^0)$, $\mathbf{u}_m^1 \in \mathcal{T}(\Omega_m^1)$, $\phi_f \in H_*^1(\Omega_f)$:

$$\begin{cases} \int_{\Omega_f} \left[(\mathbf{M}_\mu^{-1} \nabla \times \mathbf{u}_f) \cdot (\nabla \times \mathbf{v}_f) - \omega^2 (\mathbf{M}_\epsilon \mathbf{u}_f) \cdot \mathbf{v}_f \right] dx + \sum_{i=0,1} \int_{\Gamma_{f_i}} \boldsymbol{\gamma} \mathbf{u}_m^i \cdot \mathbf{v}_f dS + \int_{\Omega_f} \nabla \phi_f \cdot \mathbf{v}_f dx = \int_{\Omega_f} \mathbf{j} \cdot \mathbf{v}_f dx & \forall \mathbf{v}_f \in \mathbf{H}(\mathbf{curl}, \Omega_f), \\ \int_{\Omega_f} \mathbf{u}_f \cdot \nabla \psi_f dx - \sum_{i=0,1} \int_{\Gamma_{f_i}} (\mathbf{n} \cdot \mathbf{u}_m^i) \psi_f dS = 0 & \forall \psi_f \in H_*^1(\Omega_f). \end{cases} \quad (11)$$

⁴At first sight, one could think of combining (10a) and (10c) and impose the continuity $\mathbf{u}_f|_{\Gamma_{f_i}} = \mathbf{u}_m^i|_{\Gamma_{f_i}}$, $i = 0, 1$. However, this would only hold if each restriction of \mathbf{u} lay in $\mathbf{H}^1(\Omega_\square) := [H^1(\Omega_\square)]^3$.

In Ω_f , imposing the Coulomb gauge via the Lagrange multiplier $\phi_f \in H_*^1(\Omega_f)$ allows (10c) to hold through the boundary integrals of the second line of (11): if we set $\phi_f \in H_0^1(\Omega_f)$, such boundary integrals would in fact disappear. Conversely, the Coulomb gauge is already taken into account strongly for functions $\mathbf{u}_m^i \in \mathcal{T}(\Omega_m^i)$, $i = 0, 1$.

We end up with four different coupling approaches depending on how we impose the additional transmission condition (10a) on Γ_{f0}, Γ_{f1} and all transmission conditions (10) on Γ_{01} . These coupling approaches in the continuous and discrete cases are discussed in the following sections as stationary problems for different *Lagrangian functionals*. The resulting *linear variational saddle-point problems* are also stated.

3.1 | PDE-constrained Least-Squares Coupling

We determine a quadratic minimization problem under a linear variational constraint by seeking $\mathbf{u}_f \in \mathbf{H}(\mathbf{curl}, \Omega_f)$, $\mathbf{u}_m^0 \in \mathcal{T}(\Omega_m^0)$, and $\mathbf{u}_m^1 \in \mathcal{T}(\Omega_m^1)$ that

1. minimize the mismatch in the transmission conditions

$$\begin{aligned} J_\Gamma(\mathbf{u}_f, \mathbf{u}_m^0, \mathbf{u}_m^1) := & \|\mathbf{n} \times (\mathbf{u}_f - \mathbf{u}_m^0)\|_{\mathbf{H}^{-\frac{1}{2}}(\text{div}_{\Gamma_{f0}}, \Gamma_{f0})}^2 + \|\mathbf{n} \times (\mathbf{u}_f - \mathbf{u}_m^1)\|_{\mathbf{H}^{-\frac{1}{2}}(\text{div}_{\Gamma_{f1}}, \Gamma_{f1})}^2 + \|\mathbf{n} \times (\mathbf{u}_m^0 - \mathbf{u}_m^1)\|_{\mathbf{H}^{-\frac{1}{2}}(\text{div}_{\Gamma_{01}}, \Gamma_{01})}^2 + \\ & \|\gamma(\mathbf{u}_m^0 - \mathbf{u}_m^1)\|_{\mathbf{H}^{-\frac{1}{2}}(\text{div}_{\Gamma_{01}}, \Gamma_{01})}^2 + \|\mathbf{n} \cdot (\mathbf{u}_m^0 - \mathbf{u}_m^1)\|_{H^{-\frac{1}{2}}(\Gamma_{01})}^2 \end{aligned} \quad (12)$$

2. and satisfy the PDE-constraint (11).

Note that here the constraint is given by the variational form of the system of PDEs (1a) in Ω_f , while the functional J_Γ to be minimized is based on the transmission conditions not imposed by the variational form (11).

This problem can be rephrased as seeking a saddle point of the following Lagrangian:

$$\begin{aligned} L(\mathbf{u}_f, \mathbf{u}_m^0, \mathbf{u}_m^1, \phi_f, \mathbf{p}_f, \xi_f) := & \frac{1}{2} J_\Gamma(\mathbf{u}_f, \mathbf{u}_m^0, \mathbf{u}_m^1) + \int_{\Omega_f} [(\mathbf{M}_\mu^{-1} \nabla \times \mathbf{u}_f) \cdot (\nabla \times \mathbf{p}_f) - \omega^2 (\mathbf{M}_\epsilon \mathbf{u}_f) \cdot \mathbf{p}_f] \, dx + \sum_{i=0,1} \int_{\Gamma_{fi}} \gamma \mathbf{u}_m^i \cdot \mathbf{p}_f \, dS + \\ & \int_{\Omega_f} \nabla \phi_f \cdot \mathbf{p}_f \, dx - \int_{\Omega_f} \mathbf{j} \cdot \mathbf{p}_f + \int_{\Omega_f} \mathbf{u}_f \cdot \nabla \xi_f \, dx - \sum_{i=0,1} \int_{\Gamma_{fi}} (\mathbf{n} \cdot \mathbf{u}_m^i) \, \xi_f \, dS. \end{aligned} \quad (13)$$

- $\phi_f \in H_*^1(\Omega_f)$, as discussed in Section 1.2.
- $\mathbf{p}_f \in \mathbf{H}(\mathbf{curl}, \Omega_f)$ is the Lagrange multiplier imposing the first line of (11).
- $\xi_f \in H_*^1(\Omega_f)$ is the Lagrange multiplier imposing the second line of (11).

Saddle-Point Problem

The trace norms $\|\cdot\|_{\mathbf{H}^{-\frac{1}{2}}(\text{div}_{\Gamma_\square}, \Gamma_\square)}$, $\|\cdot\|_{H^{-\frac{1}{2}}(\Gamma_\square)}$ are nonlocal. Thus, for practicality we replace them with the $L^2(\Gamma_\square)$ and $L^2(\Gamma_\square)$ -norms in (12), respectively, and seek $\mathbf{u}_f \in \mathbf{H}_{\partial\Omega_f}(\mathbf{curl}, \Omega_f) := \left\{ \mathbf{v} \in \mathbf{H}(\mathbf{curl}, \Omega_f) : \mathbf{n} \times \mathbf{v}|_{\partial\Omega_f} \in \mathbf{L}_t^2(\partial\Omega_f) \right\}$. Given this substitution, the necessary and sufficient optimality conditions of (13) give rise to the saddle-point problem

$$\begin{aligned} \text{Seek } & \mathbf{u}_f \in \mathbf{H}_{\partial\Omega_f}(\mathbf{curl}, \Omega_f), \mathbf{u}_m^0 \in \mathcal{T}(\Omega_m^0), \mathbf{u}_m^1 \in \mathcal{T}(\Omega_m^1), \phi_f \in H_*^1(\Omega_f), \mathbf{p}_f \in \mathbf{H}(\mathbf{curl}, \Omega_f), \xi_f \in H_*^1(\Omega_f): \\ & \begin{cases} \text{a}_{\text{LS}}[(\mathbf{u}_f, \mathbf{u}_m^0, \mathbf{u}_m^1), (\mathbf{v}_f, \mathbf{v}_m^0, \mathbf{v}_m^1)] + \text{b}_{\text{LS}}[(\mathbf{v}_f, \mathbf{v}_m^0, \mathbf{v}_m^1, \psi_f), (\mathbf{p}_f, \xi_f)] = 0 \\ \text{b}_{\text{LS}}[(\mathbf{u}_f, \mathbf{u}_m^0, \mathbf{u}_m^1, \phi_f), (\mathbf{q}_f, \zeta_f)] = \int_{\Omega_f} \mathbf{j} \cdot \mathbf{q}_f \, dx \end{cases} \\ & \forall \mathbf{v}_f \in \mathbf{H}_{\partial\Omega_f}(\mathbf{curl}, \Omega_f), \forall \mathbf{v}_m^0 \in \mathcal{T}(\Omega_m^0), \forall \mathbf{v}_m^1 \in \mathcal{T}(\Omega_m^1), \forall \psi_f \in H_*^1(\Omega_f), \forall \mathbf{q}_f \in \mathbf{H}(\mathbf{curl}, \Omega_f), \forall \zeta_f \in H_*^1(\Omega_f), \end{aligned} \quad (14)$$

where

$$\begin{aligned} \text{a}_{\text{LS}}[(\mathbf{u}_f, \mathbf{u}_m^0, \mathbf{u}_m^1), (\mathbf{v}_f, \mathbf{v}_m^0, \mathbf{v}_m^1)] := & \int_{\Gamma_{f0}} [\mathbf{n} \times (\mathbf{u}_f - \mathbf{u}_m^0)] \cdot [\mathbf{n} \times (\mathbf{v}_f - \mathbf{v}_m^0)] \, dS + \int_{\Gamma_{f1}} [\mathbf{n} \times (\mathbf{u}_f - \mathbf{u}_m^1)] \cdot [\mathbf{n} \times (\mathbf{v}_f - \mathbf{v}_m^1)] \, dS + \\ & \int_{\Gamma_{01}} \left\{ [\mathbf{n} \times (\mathbf{u}_m^0 - \mathbf{u}_m^1)] \cdot [\mathbf{n} \times (\mathbf{v}_m^0 - \mathbf{v}_m^1)] + [\gamma(\mathbf{u}_m^0 - \mathbf{u}_m^1)] \cdot [\gamma(\mathbf{v}_m^0 - \mathbf{v}_m^1)] + [\mathbf{n} \cdot (\mathbf{u}_m^0 - \mathbf{u}_m^1)] \cdot [\mathbf{n} \cdot (\mathbf{v}_m^0 - \mathbf{v}_m^1)] \right\} \, dS, \end{aligned} \quad (15)$$

$$\begin{aligned} \text{b}_{\text{LS}}[(\mathbf{u}_f, \mathbf{u}_m^0, \mathbf{u}_m^1, \phi_f), (\mathbf{q}_f, \zeta_f)] := & \int_{\Omega_f} [(\mathbf{M}_\mu^{-1} \nabla \times \mathbf{u}_f) \cdot (\nabla \times \mathbf{q}_f) - \omega^2 (\mathbf{M}_\epsilon \mathbf{u}_f) \cdot \mathbf{q}_f] \, dx + \sum_{i=0,1} \int_{\Gamma_{fi}} \gamma \mathbf{u}_m^i \cdot \mathbf{q}_f \, dS + \\ & \int_{\Omega_f} \nabla \phi_f \cdot \mathbf{q}_f + \int_{\Omega_f} \mathbf{u}_f \cdot \nabla \zeta_f \, dx - \sum_{i=0,1} \int_{\Gamma_{fi}} (\mathbf{n} \cdot \mathbf{u}_m^i) \, \zeta_f \, dS. \end{aligned} \quad (16)$$

We propose the following discretization for (14):

- $\mathbf{u}_f, \mathbf{v}_f, \mathbf{p}_f, \mathbf{q}_f \in \mathbf{V}^n(\mathcal{M}_f)$, see (6a),
- $\phi_f, \psi_f, \xi_f, \zeta_f \in V^n(\mathcal{M}_f)$, see (6b),
- $\mathbf{u}_m^0, \mathbf{v}_m^0 \in \mathcal{T}^n(\Omega_m^0)$, and
- $\mathbf{u}_m^1, \mathbf{v}_m^1 \in \mathcal{T}^n(\Omega_m^1)$.

3.2 | Discontinuous Galerkin

Discontinuous Galerkin (DG) methods allow to use FEM with nonconforming meshes on different neighboring domains for the same boundary value problem [?]. This is well-suited for the coupling because one can think of MMP as FEM with special trial and test functions used on a “mesh” with two entities: Ω_m^0 and Ω_m^1 . More specifically, we want to impose weak continuity of the tangential traces (10a) by a DG method [?].

Following this idea, the coupling can be expressed as a *discrete* stationary problem for the following Lagrangian:

$$\begin{aligned} L(\mathbf{u}_f^n, \mathbf{u}_m^{n,0}, \mathbf{u}_m^{n,1}, \phi_f^n, \phi_m^{n,0}, \phi_m^{n,1}) &:= J_{\Omega_f}(\mathbf{u}_f^n, \phi_f^n) + J_{\Omega_m}(\mathbf{u}_m^{n,0}, \mathbf{u}_m^{n,1}, \phi_m^{n,0}, \phi_m^{n,1}) + \\ &\sum_{i=0,1} \int_{\Gamma_{fi}} \left[\mathbf{n} \times (\mathbf{u}_f^n - \mathbf{u}_m^{n,i}) \right] \cdot \mathbf{P}^n(\mathbf{u}_f^n, \mathbf{u}_m^{n,i}) \, dS + \int_{\Gamma_{01}} \left[\mathbf{n} \times (\mathbf{u}_m^{n,0} - \mathbf{u}_m^{n,1}) \right] \cdot \mathbf{P}^n(\mathbf{u}_m^{n,0}, \mathbf{u}_m^{n,1}) \, dS. \end{aligned} \quad (17)$$

We propose $\mathbf{u}_f^n \in \mathbf{V}^n(\mathcal{M}_f)$ (6a), $\mathbf{u}_m^{n,0} \in \mathcal{T}^n(\Omega_m^0)$, $\mathbf{u}_m^{n,1} \in \mathcal{T}^n(\Omega_m^1)$, and $\phi_f^n \in V^n(\mathcal{M}_f)$ (6b). However, to discretize $\phi_m^{n,0}, \phi_m^{n,1}$, we first need to discuss functionals $J_{\Omega_f}, J_{\Omega_m}$ in the continuous case; the discrete operator \mathbf{P}^n is discussed at a later stage.

Functionals $J_{\Omega_f}, J_{\Omega_m}$

J_{Ω_f} expresses the saddle-point problem that corresponds to (1a) in Ω_f :

$$J_{\Omega_f}(\mathbf{u}_f, \phi_f) := \frac{1}{2} \int_{\Omega_f} [(\mathbf{M}_\mu^{-1} \nabla \times \mathbf{u}_f) \cdot (\nabla \times \mathbf{u}_f) - \omega^2 (\mathbf{M}_\epsilon \mathbf{u}_f) \cdot \mathbf{u}_f] \, dx + \int_{\Omega_f} \mathbf{u}_f \cdot \nabla \phi_f \, dx - \int_{\Omega_f} \mathbf{j} \cdot \mathbf{u}_f \, dx. \quad (18a)$$

J_{Ω_m} for $\mathbf{u}_m^0, \mathbf{u}_m^1$ has a similar formulation, but for constant scalar coefficients and no sources:

$$J_{\Omega_m}(\mathbf{u}_m^0, \mathbf{u}_m^1, \phi_m^0, \phi_m^1) := \frac{1}{2} \sum_{i=0,1} \int_{\Omega_m^i} (\mu_i^{-1} \|\nabla \times \mathbf{u}_m^i\|_{\ell^2}^2 - \omega^2 \epsilon_i \|\mathbf{u}_m^i\|_{\ell^2}^2) \, dx + \sum_{i=0,1} \int_{\Omega_m^i} \mathbf{u}_m^i \cdot \nabla \phi_m^i \, dx. \quad (18b)$$

Because $\mathbf{u}_m^i \in \mathcal{T}(\Omega_m^i)$, $i = 0, 1$, one can rewrite the volume integrals in (18b) as boundary integrals:

$$\frac{1}{2} \int_{\Omega_m^i} (\mu_i^{-1} \|\nabla \times \mathbf{u}_m^i\|_{\ell^2}^2 - \omega^2 \epsilon_i \|\mathbf{u}_m^i\|_{\ell^2}^2) \, dx = -\frac{1}{2} \int_{\partial\Omega_m^i} \boldsymbol{\gamma} \mathbf{u}_m^i \cdot \mathbf{u}_m^i \, dS, \quad (19a)$$

$$\int_{\Omega_m^i} \mathbf{u}_m^i \cdot \nabla \phi_m^i \, dx = \int_{\partial\Omega_m^i} (\mathbf{n} \cdot \mathbf{u}_m^i) \phi_m^i \, dS. \quad (19b)$$

Normal Continuity

From (19b), by considering only the integrals on each $\Gamma_{fi} := \partial\Omega_f \cap \partial\Omega_m^i$, $i = 0, 1$, taking \mathbf{n} always pointing from Ω_f to Ω_m^i , and setting $\phi_m^i|_{\Gamma_{fi}} = \phi_f|_{\Gamma_{fi}}$, from (19b) one can extract the terms

$$- \sum_{i=0,1} \int_{\Gamma_{fi}} (\mathbf{n} \cdot \mathbf{u}_m^i) \phi_f \, dS, \quad (20a)$$

which is like imposing (10c) on each Γ_{fi} by inserting⁵ the MMP ansatz in the boundary terms of the second line of the variational form (4), as done in (11). Furthermore, by considering only the integrals on $\Gamma_{01} := \partial\Omega_m^0 \cap \partial\Omega_m^1$, taking the same \mathbf{n} on both sides of Γ_{01} , and defining $\phi_m^{01} := \phi_m^0|_{\Gamma_{01}} = \phi_m^1|_{\Gamma_{01}}$, from (19b) one can also extract

$$\int_{\Gamma_{01}} (\mathbf{n} \cdot \mathbf{u}_m^0 - \mathbf{n} \cdot \mathbf{u}_m^1) \phi_m^{01} \, dS, \quad (20b)$$

which is like imposing (10c) on Γ_{01} by means of a Lagrange multiplier $\phi_m^{01} \in H^{\frac{1}{2}}(\Gamma_{01})$. Thus, we can rewrite (19b) as

$$\sum_{i=0,1} \int_{\partial\Omega_m^i} (\mathbf{n} \cdot \mathbf{u}_m^i) \phi_m^i \, dS = - \sum_{i=0,1} \int_{\Gamma_{fi}} (\mathbf{n} \cdot \mathbf{u}_m^i) \phi_f \, dS + \int_{\Gamma_{01}} (\mathbf{n} \cdot \mathbf{u}_m^0 - \mathbf{n} \cdot \mathbf{u}_m^1) \phi_m^{01} \, dS. \quad (21)$$

⁵The minus sign is due to flipping the direction of \mathbf{n} , which now points from Ω_f to Ω_m^i , $i = 0, 1$, for this integral.

To discretize $\phi_m^{01} \in H^{\frac{1}{2}}(\Gamma_{01})$, we use Dirichlet traces of $\mathbf{n} \cdot \mathbf{v}_m$ on Γ_{01} , given $\mathbf{v}_m \in \mathcal{T}^n(\Omega_m^0)$ or $\mathcal{T}^n(\Omega_m^1)$, and define this discrete trace space as $\mathcal{T}^n(\Gamma_{01})$. This choice of $\mathcal{T}^n(\Gamma_{01})$ is consistent with:

- The PDE-constrained least-squares coupling approach of Section 3.1: the same test functions in $\mathcal{T}^n(\Gamma_{01})$ are chosen to impose (10c) on Γ_{01} through (12) – see (15).
- *Mortar element methods* (Section 3.3.1). In fact, these methods impose weak continuity between nonconforming meshes by a Lagrange multiplier discretized by traces of functions belonging to one of the discretization spaces of the neighboring domains, here Ω_m^0 or Ω_m^1 [?, p. 100, Remark].

Operator \mathbf{P}^n

Let us now go back to the Lagrangian functional (17). Depending on the choice of its discrete operator

$$\mathbf{P}^n : (\mathbf{V}^n(\mathcal{M}_f) + \mathcal{T}^n(\Omega_m^i)) \times (\mathbf{V}^n(\mathcal{M}_f) + \mathcal{T}^n(\Omega_m^i)) \rightarrow (\mathbf{V}^n(\mathcal{M}_f) + \mathcal{T}^n(\Omega_m^i)), \quad (22a)$$

$i = 1, 2$, we obtain different DG approaches. We follow the (symmetric) *Interior Penalty DG method* [?]:

$$\mathbf{P}^n(\mathbf{u}^n, \mathbf{v}^n) := \overline{\mathbf{M}}_\mu^{-1} [\nabla \times (\mathbf{u}^n + \mathbf{v}^n)] + \eta \overline{\mathbf{M}}_\mu^{-1} [\mathbf{n} \times (\mathbf{u}^n - \mathbf{v}^n)]. \quad (22b)$$

- $\overline{\mathbf{M}}_\mu(\mathbf{x}) : \mathbb{R}^3 \rightarrow \mathbb{C}^{3 \times 3}$ is the mean of material parameters \mathbf{M}_μ in Ω_f and Ω_m^i when integrating on each Γ_{fi} , $i = 0, 1$:

$$\overline{\mathbf{M}}_\mu(\mathbf{x}) := \frac{\mathbf{M}_\mu(\mathbf{x}) + \mu_i \mathbf{I}}{2} \quad \forall \mathbf{x} \in \Gamma_{fi}, \quad (23)$$

and of \mathbf{M}_μ in Ω_m^0 and Ω_m^1 when integrating on Γ_{01} :

$$\overline{\mathbf{M}}_\mu(\mathbf{x}) := \frac{\mu_0 + \mu_1}{2} \mathbf{I} \quad \forall \mathbf{x} \in \Gamma_{01}. \quad (24)$$

- $\eta \in \mathbb{R}$ is a penalty parameter that needs to be assigned heuristically. On any Γ_{fi} , $i = 0, 1$, η should be proportional to N_m^i/h , where N_m^i is the number of degrees of freedom of $\mathcal{T}^n(\Omega_m^i)$ and $h \in \mathbb{R}$ the meshwidth of \mathcal{M}_f restricted to Γ_{fi} . On Γ_{01} , η should be proportional to $N_m^0 + N_m^1$. Both choices are inspired by $\eta \sim p/h$, used in case of polynomial DG-FEM [?, p. 229] (with $p \in \mathbb{N}^*$ the polynomial degree).

Saddle-Point Problem

Finding the stationary point of (17) leads to the discrete saddle-point problem

$$\begin{aligned} \text{Seek } & \mathbf{u}_f^n \in \mathbf{V}^n(\mathcal{M}_f), \mathbf{u}_m^{n,0} \in \mathcal{T}^n(\Omega_m^0), \mathbf{u}_m^{n,1} \in \mathcal{T}^n(\Omega_m^1), \phi_f^n \in V^n(\mathcal{M}_f), \phi_m^{n,01} \in \mathcal{T}^n(\Gamma_{01}): \\ & \begin{cases} a_{\text{DG}}^n[(\mathbf{u}_f^n, \mathbf{u}_m^{n,0}, \mathbf{u}_m^{n,1}), (\mathbf{v}_f^n, \mathbf{v}_m^{n,0}, \mathbf{v}_m^{n,1})] + b_{\text{DG}}^n[(\mathbf{v}_f^n, \mathbf{v}_m^{n,0}, \mathbf{v}_m^{n,1}), (\phi_f^n, \phi_m^{n,01})] = \int_{\Omega_f} \mathbf{j} \cdot \mathbf{v}_f^n \, dx \\ b_{\text{DG}}^n[(\mathbf{u}_f^n, \mathbf{u}_m^{n,0}, \mathbf{u}_m^{n,1}), (\psi_f^n, \psi_m^{n,01})] = 0 \end{cases} \\ & \forall \mathbf{v}_f^n \in \mathbf{V}^n(\mathcal{M}_f), \forall \mathbf{v}_m^{n,0} \in \mathcal{T}^n(\Omega_m^0), \forall \mathbf{v}_m^{n,1} \in \mathcal{T}^n(\Omega_m^1), \forall \psi_f^n \in V^n(\mathcal{M}_f), \forall \psi_m^{n,01} \in \mathcal{T}^n(\Gamma_{01}), \end{aligned} \quad (25)$$

where we define the symmetric bilinear form $a_{\text{DG}}^n(\cdot, \cdot)$ and linear form $b_{\text{DG}}^n(\cdot, \cdot)$ as

$$\begin{aligned} a_{\text{DG}}^n [(\mathbf{u}_f^n, \mathbf{u}_m^{n,0}, \mathbf{u}_m^{n,1}), (\mathbf{v}_f^n, \mathbf{v}_m^{n,0}, \mathbf{v}_m^{n,1})] &:= \int_{\Omega_f} [(\overline{\mathbf{M}}_\mu^{-1} \nabla \times \mathbf{u}_f^n) \cdot (\nabla \times \mathbf{v}_f^n) - \omega^2 (\mathbf{M}_\epsilon \mathbf{u}_f^n) \cdot \mathbf{v}_f^n] \, dx + \\ & \sum_{i=0,1} \int_{\Gamma_{fi}} \left\{ [\overline{\mathbf{M}}_\mu^{-1} \nabla \times (\mathbf{u}_f^n + \mathbf{u}_m^{n,i})] \cdot [\mathbf{n} \times (\mathbf{v}_f^n - \mathbf{v}_m^{n,i})] + [\mathbf{n} \times (\mathbf{u}_f^n - \mathbf{u}_m^{n,i})] \cdot [\overline{\mathbf{M}}_\mu^{-1} \nabla \times (\mathbf{v}_f^n + \mathbf{v}_m^{n,i})] \right\} \, dS + \\ & \sum_{i=0,1} \int_{\Gamma_{fi}} 2\eta [\overline{\mathbf{M}}_\mu^{-1} \mathbf{n} \times (\mathbf{u}_f^n - \mathbf{u}_m^{n,i})] \cdot [\mathbf{n} \times (\mathbf{v}_f^n - \mathbf{v}_m^{n,i})] \, dS - \sum_{i=0,1} \int_{\partial\Omega_m^i} \gamma \mathbf{u}_m^{n,i} \cdot \mathbf{v}_m^{n,i} \, dS + \\ & \int_{\Gamma_{01}} \left\{ [\overline{\mathbf{M}}_\mu^{-1} \nabla \times (\mathbf{u}_m^{n,0} + \mathbf{u}_m^{n,1})] \cdot [\mathbf{n} \times (\mathbf{v}_m^{n,0} - \mathbf{v}_m^{n,1})] + [\mathbf{n} \times (\mathbf{u}_m^{n,0} - \mathbf{u}_m^{n,1})] \cdot [\overline{\mathbf{M}}_\mu^{-1} \nabla \times (\mathbf{v}_m^{n,0} + \mathbf{v}_m^{n,1})] \right\} \, dS + \\ & \int_{\Gamma_{01}} 2\eta [\overline{\mathbf{M}}_\mu^{-1} \mathbf{n} \times (\mathbf{u}_m^{n,0} - \mathbf{u}_m^{n,1})] \cdot [\mathbf{n} \times (\mathbf{v}_m^{n,0} - \mathbf{v}_m^{n,1})] \, dS, \end{aligned} \quad (26)$$

$$\begin{aligned} b_{\text{DG}}^n [(\mathbf{u}_f^n, \mathbf{u}_m^{n,0}, \mathbf{u}_m^{n,1}), (\psi_f^n, \psi_m^{n,01})] &:= \int_{\Omega_f} \mathbf{u}_f^n \cdot \nabla \psi_f^n \, dx - \\ & \int_{\Gamma_{00}} (\mathbf{n} \cdot \mathbf{u}_m^{n,0}) \psi_f^n \, dS - \int_{\Gamma_{01}} (\mathbf{n} \cdot \mathbf{u}_m^{n,1}) \psi_f^n \, dS + \int_{\Gamma_{01}} (\mathbf{n} \cdot \mathbf{u}_m^{n,0} - \mathbf{n} \cdot \mathbf{u}_m^{n,1}) \psi_m^{n,01} \, dS. \end{aligned} \quad (27)$$

3.3 | Coupling by Tangential Components Traces

The two coupling approaches we describe now can only be used in the case of $m = 0$, i.e. a single (unbounded) Trefftz domain Ω_m^0 , which we refer to as Ω_m . This also results in having a single interface $\Gamma \equiv \Gamma_{f_0} = \partial\Omega_f = \partial\Omega_m$.

Moreover, both these methods

1. impose the continuity of the *tangential components trace* for Maxwell's equations (1), i.e.

$$\mathbf{n} \times (\mathbf{n} \times \mathbf{u}_f)|_{\Gamma} = \mathbf{n} \times (\mathbf{n} \times \mathbf{u}_m)|_{\Gamma}, \quad (28)$$

instead of the continuity between tangential traces stated in (10a), and

2. enforce (28) weakly through test functions $\gamma \mathbf{v}$, given $\mathbf{v} \in \mathbf{H}_{\text{loc}}(\mathbf{curl}, \Omega_{\square})$, $\Omega_{\square} \in \{\Omega_f, \Omega_m\}$.

3.3.1 | Multi-Field Coupling

As for the DG-based coupling (Section 3.2), we treat the (here single) MMP discretization as a finite element with special functions. However, now we rely on the other main approach for imposing weak continuity on nonconforming meshes, which is the *multi-field domain decomposition method* [?].

For Maxwell's equations, the multi-field method aims at imposing the continuity of the tangential components trace (28) in a weak sense by means of a Lagrange multiplier

$$\boldsymbol{\lambda} := \gamma \mathbf{v}, \quad \mathbf{v} \in \mathbf{H}_{\text{loc}}(\mathbf{curl}, \Omega), \quad \Omega \subseteq \mathbb{R}^3. \quad (29)$$

From (29) one can see that $\boldsymbol{\lambda}$ belongs to the dual space $\mathbf{H}^{-\frac{1}{2}}(\text{div}_{\Gamma}, \Gamma)$, which is consistent with (28) connecting traces in $\mathbf{H}^{-\frac{1}{2}}(\mathbf{curl}_{\Gamma}, \Gamma)$.

The rationale behind the multi-field method becomes clear if one applies the generalized Stokes' theorem in $\mathbf{H}(\mathbf{curl} \mathbf{curl}, \Omega)$ to the weak form of (1a) in Ω_f , which then leads to the boundary integral

$$\int_{\Gamma} \gamma \mathbf{u}_f \cdot [\mathbf{n} \times (\mathbf{n} \times \mathbf{v}_f)] \, dS. \quad (30)$$

Substituting (28) into (30), we can understand the reason for (29). Then, relying on the definition of γ (5), (30) can be simplified as the boundary integrals of the first line of (11).

Hence, the multi-field coupling can be expressed by the following Lagrangian:

$$L(\mathbf{u}_f, \mathbf{u}_m, \phi_f, \phi_m, \boldsymbol{\lambda}) := J_{\Omega_f}(\mathbf{u}_f, \phi_f) + J_{\Omega_m}(\mathbf{u}_m, \phi_m) + \int_{\Gamma} \{\mathbf{n} \times [\mathbf{n} \times (\mathbf{u}_f - \mathbf{u}_m)]\} \cdot \boldsymbol{\lambda} \, dS, \quad (31)$$

where J_{Ω_f} and J_{Ω_m} are the same as in (18a) and (18b). In the same way as (19), we can also rewrite the volume integrals of J_{Ω_m} as boundary integrals on the single interface Γ and then, as in (20a), rename $\phi_m|_{\Gamma}$ as $\phi_f|_{\Gamma}$.

Saddle-Point Problem

We obtain the following saddle-point problem:

$$\begin{aligned} & \text{Seek } \mathbf{u}_f \in \mathbf{H}(\mathbf{curl}, \Omega_f), \mathbf{u}_m \in \mathcal{T}(\Omega_m), \phi_f \in H_*^1(\Omega_f), \boldsymbol{\lambda} \in \tilde{\mathbf{H}}^{-\frac{1}{2}}(\text{div}_{\Gamma}, \Gamma): \\ & \begin{cases} \mathbf{a}_{\text{MF}}[(\mathbf{u}_f, \mathbf{u}_m), (\mathbf{v}_f, \mathbf{v}_m)] + \mathbf{b}_{\text{MF}}[(\mathbf{v}_f, \mathbf{v}_m), (\phi_f, \boldsymbol{\lambda})] = \int_{\Omega_f} \mathbf{j} \cdot \mathbf{v}_f \, dx \\ \mathbf{b}_{\text{MF}}[(\mathbf{u}_f, \mathbf{u}_m), (\psi_f, \boldsymbol{\chi})] = 0 \end{cases} \\ & \forall \mathbf{v}_f \in \mathbf{H}(\mathbf{curl}, \Omega_f), \forall \mathbf{v}_m \in \mathcal{T}(\Omega_m), \forall \psi_f \in H_*^1(\Omega_f), \forall \boldsymbol{\chi} \in \tilde{\mathbf{H}}^{-\frac{1}{2}}(\text{div}_{\Gamma}, \Gamma), \end{aligned} \quad (32)$$

where

$$\mathbf{a}_{\text{MF}}[(\mathbf{u}_f, \mathbf{u}_m), (\mathbf{v}_f, \mathbf{v}_m)] := \int_{\Omega_f} [(\mathbf{M}_{\mu}^{-1} \nabla \times \mathbf{u}_f) \cdot (\nabla \times \mathbf{v}_f) - \omega^2 (\mathbf{M}_{\epsilon} \mathbf{u}_f) \cdot \mathbf{v}_f] \, dx - \int_{\Gamma} \gamma \mathbf{u}_m \cdot \mathbf{v}_m \, dS, \quad (33a)$$

$$\mathbf{b}_{\text{MF}}[(\mathbf{u}_f, \mathbf{u}_m), (\psi_f, \boldsymbol{\chi})] := \int_{\Omega_f} \mathbf{u}_f \cdot \nabla \psi_f \, dx - \int_{\Gamma} (\mathbf{n} \cdot \mathbf{u}_m) \psi_f \, dS + \int_{\Gamma} \{\mathbf{n} \times [\mathbf{n} \times (\mathbf{u}_f - \mathbf{u}_m)]\} \cdot \boldsymbol{\chi} \, dS. \quad (33b)$$

For the discretization of (32), we suggest $\mathbf{u}_f, \mathbf{v}_f \in \mathbf{V}^n(\mathcal{M}_f)$ of (6a), $\phi_f, \psi_f \in V^n(\mathcal{M}_f)$ of (6b), and $\mathbf{u}_m, \mathbf{v}_m \in \mathcal{T}^n(\Omega_m)$, as in Sections 3.1 and 3.2. Conversely, the discretization of $\boldsymbol{\lambda} \in \tilde{\mathbf{H}}^{-\frac{1}{2}}(\text{div}_{\Gamma}, \Gamma)$ is a topic debated in the literature [?, Section 4]. In the spirit of *mortar element methods*, we opt for the tangential traces on Γ of the trial space used to discretize one of the neighboring domains [?, p. B426], specifically the Nédélec's space $\mathbf{V}^n(\mathcal{M}_f)$, given its higher number of degrees of freedom than $\mathcal{T}^n(\Omega_m)$.

Note that this choice, while being the most common discretization strategy [?, Section 4.1], ignores the duality of λ . This nonconforming discretization then prevents us from extending the multi-field coupling approach to the case with multiple MMP domains. As a matter of fact, a Lagrange multiplier $\lambda_{01} \in \tilde{\mathbf{H}}^{-\frac{1}{2}}(\text{div}_{\Gamma_{01}}, \Gamma_{01})$, which would impose continuity of tangential components traces between the MMP domains Ω_m^0, Ω_m^1 , would have to be discretized by the tangential traces of either $\mathcal{T}^n(\Omega_m^0)$ or $\mathcal{T}^n(\Omega_m^1)$, the neighboring volume discretization spaces. While on Γ_{f0} and Γ_{f1} the Nédélec's space is the obvious natural decision, no easy choice exists on Γ_{01} .

This is a similar issue that afflicts the discretization of $\psi_m^{n,01}$ for the DG-based coupling (Section 3.2). However, in that case only the normal continuity (10c) between MMP domains is affected, which is of lesser importance because it comes from a Gauge condition (second line of (1a)). On the other hand, the tangential continuity (10a) comes from the physically more relevant Maxwell's equations (first line of (1a)).

3.3.2 | Dirichlet-to-Neumann-based Coupling

This coupling approach is a special case of the *Trefftz co-chain calculus* presented in [?], where Trefftz methods are coupled with any numerical method based on volume meshes that fits the framework of co-chain calculus. Obviously, the numerical method here is FEM.

As mentioned in Section 3.3, instead of the continuity between tangential traces implied by (10a), we take into account the continuity of the tangential components trace. (28) is then imposed in weak form by testing it with $\gamma \mathbf{v}_m$, given $\mathbf{v}_m \in \mathcal{T}(\Omega_m)$ (compare with (29) and (30) in Section 3.3.1):

$$\int_{\Gamma} \{[\mathbf{n} \times (\mathbf{n} \times \mathbf{u}_f)] - [\mathbf{n} \times (\mathbf{n} \times \mathbf{u}_m)]\} \cdot \gamma \mathbf{v}_m \, dS = 0 \implies \int_{\Gamma} (\mathbf{u}_f - \mathbf{u}_m) \cdot \gamma \mathbf{v}_m \, dS = 0 \quad \forall \mathbf{v}_m \in \mathcal{T}(\Omega_m), \quad (34)$$

which holds because of the definition of γ (5).

Saddle-Point Problem

Combining (34) with the (symmetrized) variational form (11), we end up with the following system:

$$\begin{aligned} & \text{Seek } \mathbf{u}_f \in \mathbf{H}(\mathbf{curl}, \Omega_f), \mathbf{u}_m \in \mathcal{T}(\Omega_m), \phi_f \in H_*^1(\Omega_f): \\ & \begin{cases} a_{\text{DTN}}[(\mathbf{u}_f, \mathbf{u}_m), (\mathbf{v}_f, \mathbf{v}_m)] + b_{\text{DTN}}[(\mathbf{v}_f, \mathbf{v}_m), \phi_f] = \int_{\Omega_f} \mathbf{j} \cdot \mathbf{v}_f \, dx \\ b_{\text{DTN}}[(\mathbf{u}_f, \mathbf{u}_m), \psi_f] = 0 \end{cases} \\ & \forall \mathbf{v}_f \in \mathbf{H}(\mathbf{curl}, \Omega_f), \forall \mathbf{v}_m \in \mathcal{T}(\Omega_m), \forall \psi_f \in H_*^1(\Omega_f), \end{aligned} \quad (35)$$

where

$$a^{\text{DTN}}[(\mathbf{u}_f, \mathbf{u}_m), (\mathbf{v}_f, \mathbf{v}_m)] := \int_{\Omega_f} [(\mathbf{M}_\mu^{-1} \nabla \times \mathbf{u}_f) \cdot (\nabla \times \mathbf{v}_f) - \omega^2 (\mathbf{M}_\epsilon \mathbf{u}_f) \cdot \mathbf{v}_f] \, dx + \int_{\Gamma} \mathbf{u}_f \cdot \gamma \mathbf{v}_m \, dS + \int_{\Gamma} \gamma \mathbf{u}_m \cdot \mathbf{v}_f \, dS - \int_{\Gamma} \gamma \mathbf{u}_m \cdot \mathbf{v}_m \, dS, \quad (36a)$$

$$b^{\text{DTN}}[(\mathbf{u}_f, \mathbf{u}_m), \psi_f] := \int_{\Omega_f} \mathbf{u}_f \cdot \nabla \psi_f \, dx - \int_{\Gamma} (\mathbf{n} \cdot \mathbf{u}_m) \psi_f \, dS. \quad (36b)$$

The Galerkin discretization of (35) is straightforward: as done before, we replace $\mathbf{H}(\mathbf{curl}, \Omega_f)$ with $\mathbf{V}^n(\mathcal{M}_f)$ of (6a), $H^1(\Omega_f)$ with $V^n(\mathcal{M}_f)$ of (6b), and $\mathcal{T}(\Omega_m)$ with a finite-dimensional subspace $\mathcal{T}^n(\Omega_m)$.

Note that (35) can also be derived by finding a stationary point of the functional

$$L(\mathbf{u}_f, \mathbf{u}_m, \phi_f, \phi_m) := J_{\Omega_f}(\mathbf{u}_f, \phi_f) + J_{\Omega_m}(\mathbf{u}_m, \phi_m) + \int_{\Gamma} \mathbf{u}_f \cdot \gamma \mathbf{u}_m \, dS, \quad (37)$$

where J_{Ω_f} and J_{Ω_m} are the same as in (18a) and (18b) and ϕ_m disappears by setting $\phi_m|_{\Gamma} = \phi_f|_{\Gamma}$ as in (20a).

4 | NUMERICAL RESULTS

Throughout we use lowest-order $\mathbf{H}(\mathbf{curl}, \Omega_f)$ -conforming edge elements of the first family due to Nédélec for vector variables, i.e. $\mathbf{V}^n(\mathcal{M}_f) = \mathcal{R}^1(\mathcal{M}_f)$ from (6a), and piecewise-linear Lagrangian finite elements for scalar variables, i.e. $V^n(\mathcal{M}_f) = \mathcal{S}_1^0(\mathcal{M}_f)$ from (6b). Unstructured meshes \mathcal{M}_f of Ω_f are composed of tetrahedra.

To study the convergence we employ uniform h -refinement of \mathcal{M}_f and p -refinement of the Trefftz (MMP) approximations, in the sense that we increase the number of multipoles. The p -refinement of the multipoles forming $\mathcal{T}^n(\Omega_m^i)$, $i = 0, 1$, is linked to the h -refinement of \mathcal{M}_f ; specifically, to the logarithm of the number of intersections of the mesh entities of \mathcal{M}_f on Γ_{fi} . This choice is motivated by the exponential convergence of the MMP approximation error (see Section 2.2). Hence, in the next pages (log-log) plots of the results will show the algebraic convergence characteristic of h -FEM: rates are fitted with the `polyfit` function of MATLAB (degree 1) applied to log-transformed data.

We monitor the following errors:

- The volume error in the bounded domains Ω_f, Ω_m^1 . These are the relative $\mathbf{L}^2(\Omega_f)$ - and $\mathbf{L}^2(\Omega_m^1)$ -errors of the FEM and MMP (in Ω_m^1) approximations compared to the reference solution \mathbf{u} , i.e.

$$\left\| \mathbf{u} - \sum_{j=1}^{N_f} \alpha_f^j \mathbf{v}_f^j(\mathbf{x}) \right\|_{\mathbf{L}^2(\Omega_f)} / \|\mathbf{u}\|_{\mathbf{L}^2(\Omega_f)} \quad \text{and} \quad \left\| \mathbf{u} - \sum_{j=1}^{N_m^1} \alpha_m^{j,1} \mathbf{v}_m^{j,1}(\mathbf{x}) \right\|_{\mathbf{L}^2(\Omega_m^1)}^2 / \|\mathbf{u}\|_{\mathbf{L}^2(\Omega_m^1)}, \quad (38)$$

with $\alpha_f^j, \alpha_m^{j,1} \in \mathbb{C}$, $\mathbf{v}_f^j \in \mathbf{V}^n(\mathcal{M}_f)$, $\mathbf{v}_m^{j,1} \in \mathcal{T}^n(\Omega_m^1)$, and N_f, N_m^1 numbers of degrees of freedom of the discrete spaces $\mathbf{V}^n(\mathcal{M}_f)$ and $\mathcal{T}^n(\Omega_m^1)$, respectively.

On the bounded MMP domain Ω_m^1 we define an auxiliary volume mesh for the numerical quadrature of the error (38). However, on top of \mathcal{M}_f , only a mesh on the 2-dimensional hypersurface Γ_{01} is really necessary for the coupling, in order to compute the numerical integrals on that interface. Specifically, throughout we mesh Γ_{01} (and any curved surface) by simple polyhedral approximations. Of course, if only one (unbounded) MMP domain Ω_m is considered, then only the mesh \mathcal{M}_f is needed (and no other volume error than $\mathbf{L}^2(\Omega_f)$ is computed).

- The boundary error on $\partial\Omega_m^0 = \Gamma_{f0} \cup \Gamma_{01}$, union of the interfaces between the unbounded domain Ω_m^0 and the other (bounded) domains Ω_f, Ω_m^1 . This is the relative $\mathbf{L}^2(\partial\Omega_m^0)$ -error of the MMP solution in Ω_m^0 compared to the reference solution.

We can ignore the impact of numerical integration for FEM because we use a local Gaussian quadrature rule that is exact for polynomials of degree 2 (order 3).

4.0.1 | Implementation

Meshes were generated using COMSOL v5.3a.

Our code is written in C++. We use Eigen v3.3.7 for linear algebra and HyDi for the FEM component. HyDi, which can handle Hybrid nonconforming meshes and Discontinuous finite elements, is a template-based C++14 library, parallelized with C++11 multithreading, that is used as in-house simulation software at the multinational ABB [?, p. 147, Chapter 6].

Finally, the PARDISO v6.0 solver provides the sparse LU decomposition to solve the systems of the FEM-MMP coupling, characterized by nontrivial sparsity patterns.

4.1 | Electromagnetic Wave Propagation with Exact Solution

We solve $\nabla \times (\mu^{-1} \nabla \times \mathbf{u}) - \omega^2 \epsilon \mathbf{u} = \mathbf{0}$, $\nabla \cdot \mathbf{u} = 0$ in \mathbb{R}^3 subject to the Silver-Müller radiation condition (1b) with piecewise-constant permeability $\mu = 2.5281 \mu_0$ in a unit ball centered in the origin, which we dub Ω_\bullet , and $\mu = \mu_0 = 4\pi \cdot 10^{-7} \text{ H s}^{-1}$ (permeability of free space) elsewhere. ϵ and ω are everywhere equal to $\epsilon_0 = 8.85 \cdot 10^{-12} \text{ F m}^{-1}$ (permittivity of free space) and $23.56 \cdot 10^8 \text{ rad s}^{-1}$, respectively. Wavenumbers are therefore $k_\bullet = 1.59 k_0$ in Ω_\bullet and $k_0 = 7.86 \text{ rad m}^{-1}$ elsewhere.

We assume that \mathbf{u} is subject to an excitation by an incident plane wave propagating along the z -axis outside Ω_\bullet , i.e.

$$\mathbf{u} = \mathbf{u}_{\text{inc}} + \mathbf{u}_{\text{ref}} \text{ in } \mathbb{R}^3 \setminus \Omega_\bullet, \quad \mathbf{u}_{\text{inc}} := \exp(ik_0 z) (0, 1, 0)^\top, \quad (39)$$

where \mathbf{u}_{ref} represents the unknown reflected potential and z in \mathbf{u}_{inc} the third Cartesian coordinate. This problem has an exact solution coming from *Mie theory* [?, Chapter 4, pp. 82–101], where the plane wave is expanded into vector spherical harmonics and coefficients are derived for the corresponding terms of the expansions of the reflected and transmitted potentials.

For our numerical tests, we consider the terms in the expansions of Mie theory for $\ell = 1, \dots, 5$ (35 terms), identify Ω_\bullet with Ω_f and $\mathbb{R}^3 \setminus \Omega_\bullet$ with a single MMP domain Ω_m , and therefore set $\Gamma := \partial\Omega_f \cap \partial\Omega_m$ on the physical boundary of the ball. Given that we use tetrahedral meshes, Γ is actually a polyhedral approximation of a sphere.

Note that in this setting \mathbf{u}_m has an analytic extension beyond Ω_m , and hence fulfills the requirements for exponential convergence (Section 2.2). $\mathcal{T}^n(\Omega_m)$ is then generated by a single multipole expansion centered in the origin.

Numerical Results (One Trefftz Domain)

Figure 2 exemplifies the performance of FEM-MMP by visualizing the magnitude of \mathbf{u} in the case of the DtN-based coupling (Section 3.3.2) compared to the exact solution. The other coupling schemes return comparable images.

For a quantitative convergence test, see Figure 3, which shows h -refinement convergence plots for all coupling approaches, which yield very similar results. We can clearly see algebraic convergence of the FEM and MMP errors.

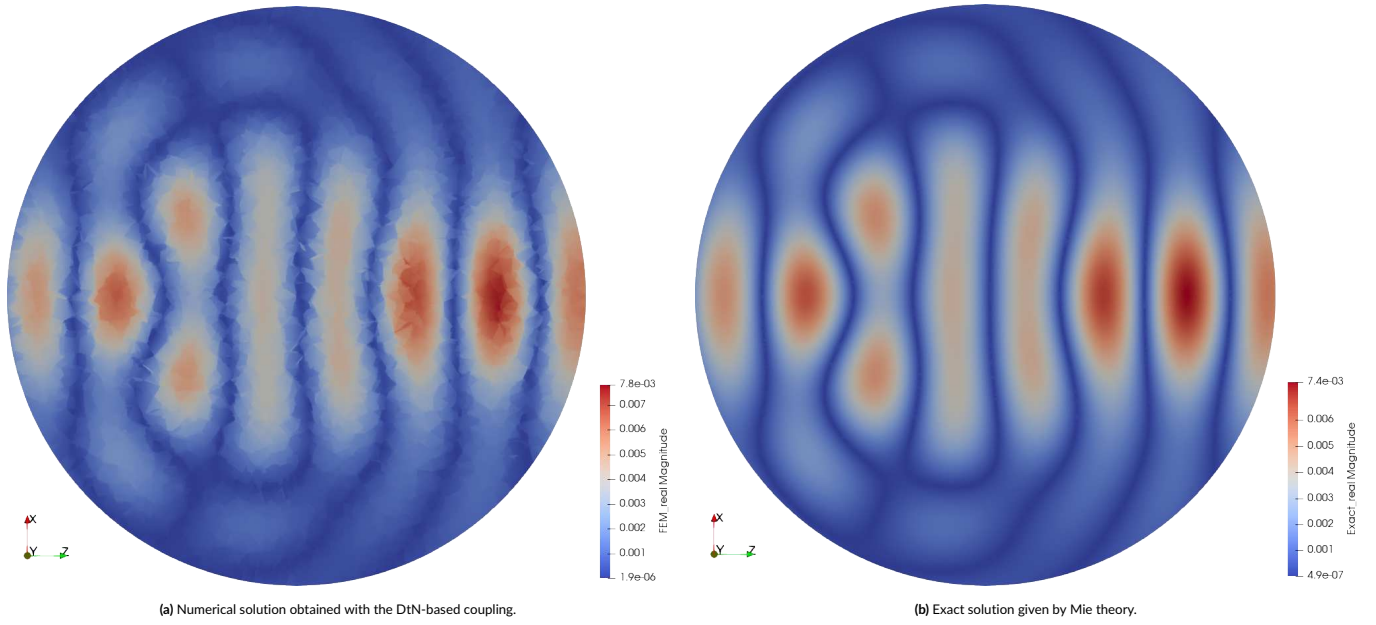


FIGURE 2 Magnitude of the real component of \mathbf{u} along the XZ -plane for $\mu_\bullet = 2.5281 \mu_0$ and $\omega = 23.56 \cdot 10^8 \text{ rad s}^{-1}$. The excitation is given by the expansion of a plane wave in terms of vector spherical harmonics (for $\ell = 1, \dots, 5$) propagating along the z -axis. Artifacts in Figure 2a are due to the numerical solution being linked to a mesh.

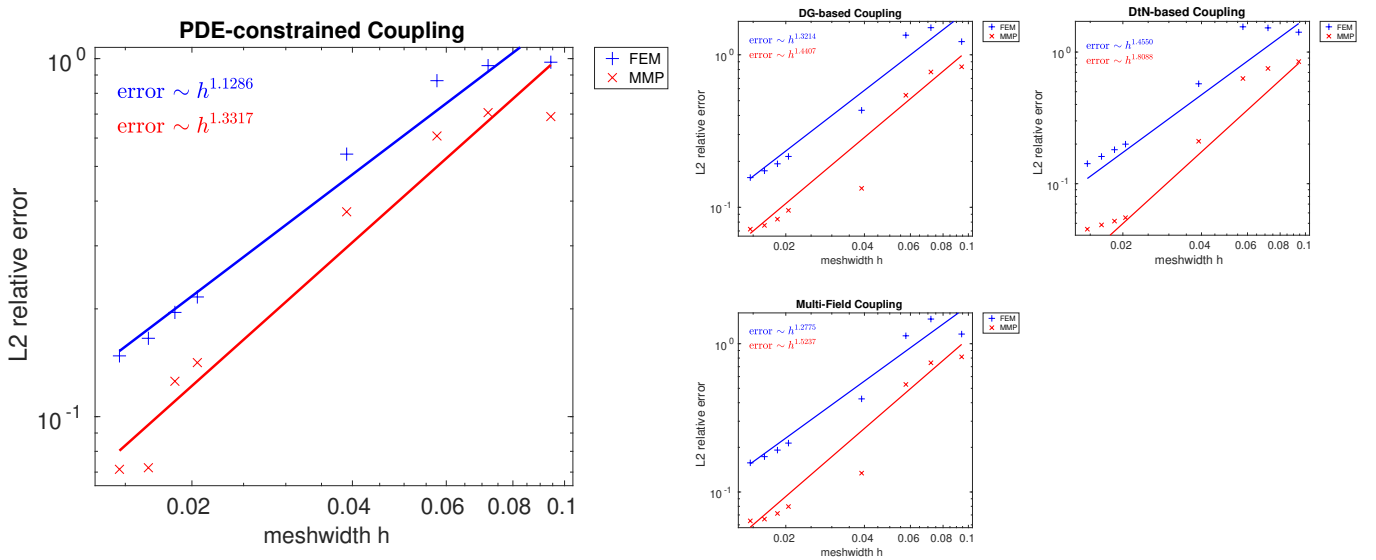


FIGURE 3 h -refinement log-log error plots for time-harmonic Maxwell's equations with exact solution. Parameters are $\mu_\bullet = 2.5281 \mu_0$ and $\omega = 23.56 \cdot 10^8 \text{ rad s}^{-1}$.

Figure 4 shows surface plots of the total relative L^2 -error for all coupling approaches. The error decreases with h (algebraic convergence) and is generally independent from the number of multipoles: the FEM error dominates. This is a consequence of the exponential convergence of MMP (Section 2.2): the exact solution is so easy to approximate in the MMP domain that it can already be represented by a multipole expansion of the lowest considered order, which is 8, leading to 160 terms of the expansion – see (8).

However, the error also increases when switching to coarser meshes and larger numbers of multipoles, when the coupling is mostly difficult due to a disproportionately high number of degrees of freedom for MMP (dense blocks of the coupling matrices) with respect to FEM (sparse blocks).

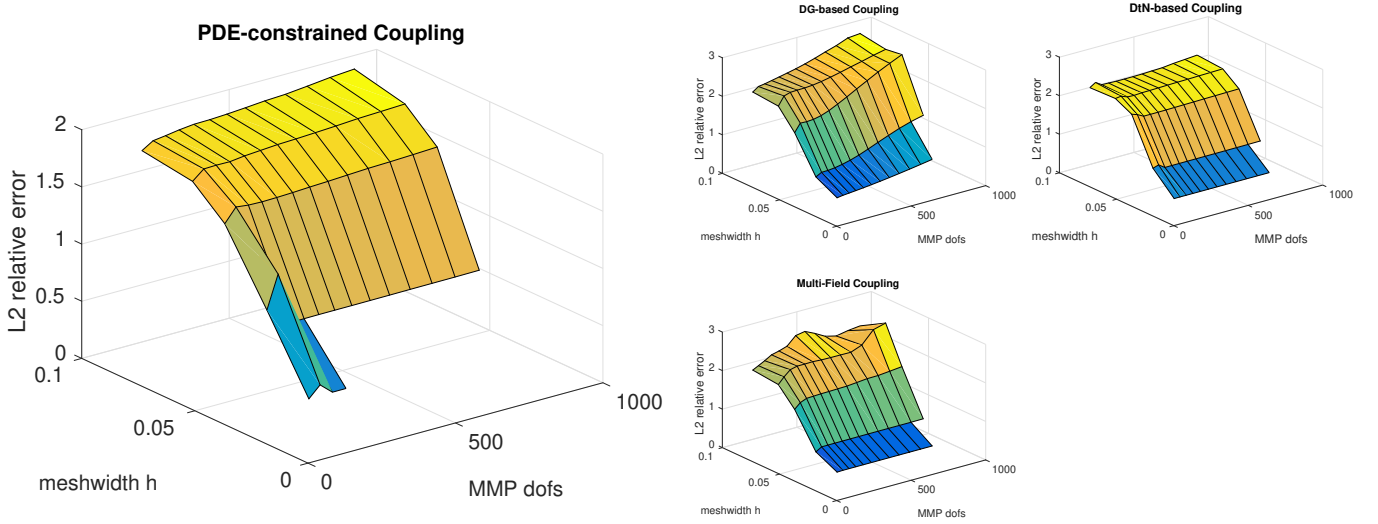


FIGURE 4 Meshwidth h vs. MMP degrees of freedom for time-harmonic Maxwell's equations with exact solution: total relative error. Parameters are $\mu_\bullet = 2.5281 \mu_0$ and $\omega = 23.56 \cdot 10^8 \text{ rad s}^{-1}$.

In these cases, our conjecture is that it becomes difficult for a direct solver to properly solve such an ill-conditioned system, and the MMP error dominates.

Moreover, we do not have datapoints for the PDE-constrained coupling with the most refined meshes and highest numbers of multipoles: the resulting linear systems are too large to be solved by an LU decomposition due to memory constraints.

4.1.1 | Two Trefftz Domains

Parameters are still $\mu_\bullet = 2.5281 \mu_0$, $\epsilon_\bullet = \epsilon_0$, and $\omega = 23.56 \cdot 10^8 \text{ rad s}^{-1}$. We split the unit ball Ω_\bullet into two halves, one modeled by FEM (Ω_f), the other by MMP (Ω_m^1): the coupling interface Γ_{f1} is therefore artificial. MMP also models the complement $\mathbb{R}^3 \setminus \Omega_\bullet$ (Ω_m^0): the coupling boundaries Γ_{f0} and Γ_{01} , on the two halves of the sphere, correspond to the physical discontinuity of μ .

As excitation, we consider terms for $\ell = 1, \dots, 5$ from the expansion of a plane wave given by Mie theory.

In this setting \mathbf{u}_m^0 and \mathbf{u}_m^1 again have analytic extensions beyond Ω_m^0 and Ω_m^1 , and hence fulfill the requirements for exponential convergence (Section 2.2). To approximate in Ω_m^1 , a single multipole expansion with spherical Bessel functions as radial dependence is centered in the origin: Bessel functions of the first kind have no singularities in that point, which lies on $\partial\Omega_m^1$. To approximate in Ω_m^0 , a single multipole expansion with spherical Hankel functions as radial dependence is also centered in the origin.

Figure 5 shows h -refinement convergence plots for all coupling approaches that work with multiple MMP domains (Sections 3.1 and 3.2). We can see algebraic convergence of the FEM and MMP errors, which is of rate ~ 1 for FEM.

4.2 | Electromagnetic Wave Propagation with Triple-Point Singularities

The problem is the same as in Section 4.1, but now we consider different values of μ in each half of the ball Ω_\bullet . Specifically, we take $\mu_+ = 4 \mu_0$ in one half of Ω_\bullet and $\mu_- = 2.5281 \mu_0$ in the other half. ω is still $= 23.56 \cdot 10^8 \text{ rad s}^{-1}$: wavenumbers are $k_+ = 2 k_0$ and $k_- = 1.59 k_0$. Hence, on the circumference that delimits the surface splitting Ω_\bullet , we have triple-point singularities.

We fully surround the circumference with TPS by a mesh, and therefore also model with FEM a small region on the other side of the physical discontinuity of Ω_\bullet , and an "airbox" in $\mathbb{R}^3 \setminus \Omega_\bullet$. The coupling interfaces Γ_{f0} and Γ_{f1} are therefore auxiliary; only the interface Γ_{01} is physical. The FEM mesh is also locally refined towards the points with TPS. A sample mesh is shown in Figure 6.

The excitation is still given by a plane wave $\mathbf{u}_{\text{inc}} := \exp(ik_0 z) (0, 1, 0)^\top$ that shifts the MMP ansatz in Ω_m^0 . However, given the TPS, there is no exact solution: as reference we rely on the numerical solution provided by a mesh substantially more refined than the finest mesh used in the convergence study.

To approximate in Ω_m^1 , a single multipole expansion with spherical Bessel functions as radial dependence is centered in the origin. To approximate in Ω_m^0 , a single multipole expansion with spherical Hankel functions as radial dependence is also centered in the origin.

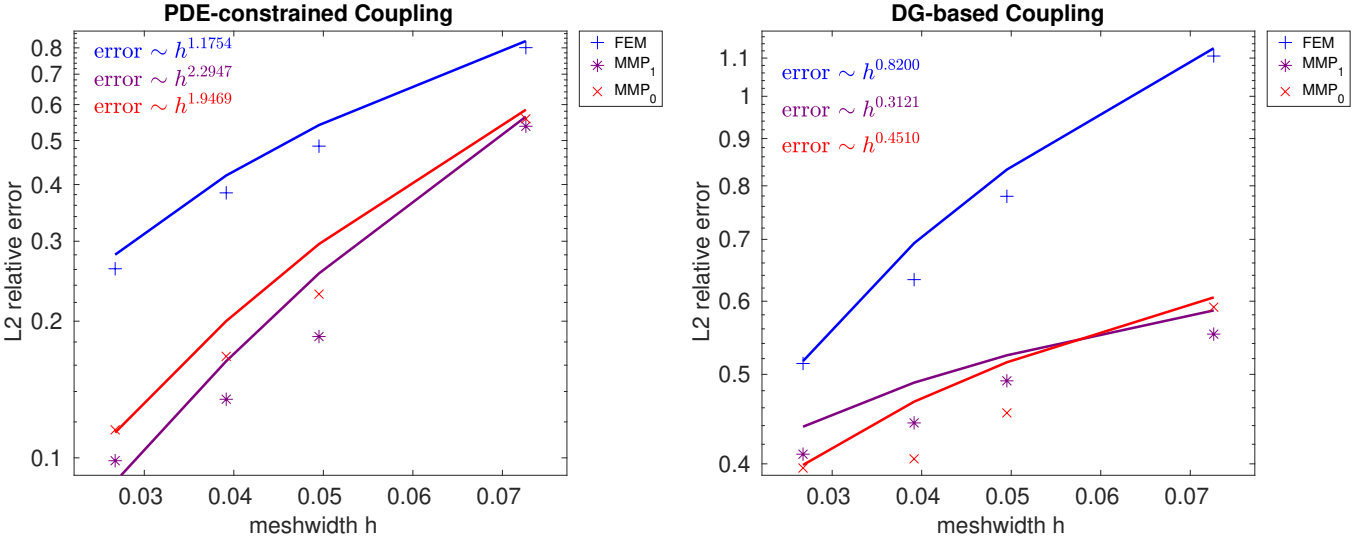


FIGURE 5 h -refinement semi-log error plots (y -axis) for time-harmonic Maxwell's equations with exact solution solved with two MMP domains. Parameters are $\mu_{\bullet} = 2.5281 \mu_0$ and $\omega = 23.56 \cdot 10^8 \text{ rad s}^{-1}$.

Numerical Results

Figure 7 shows DoF-refinement convergence plots for all coupling approaches that work with multiple MMP domains. We can clearly see algebraic convergence of the FEM and MMP errors, even if the relative errors of the DG-based coupling are higher than those of the PDE-constrained approach.

We have also considered material parameters where the frequency ω is lower, and therefore FEM suffers less from the pollution effect, but the difference between μ_+ , μ_- , and μ_0 is higher and the TPS more pronounced. Specifically, $\mu_+ = 10 \mu_0$, $\mu_- = 4 \mu_0$, and $\omega = 23.56 \cdot 10^7 \text{ rad s}^{-1}$.

Figure 8 shows DoF-refinement convergence plots for all coupling approaches that work with multiple MMP domains. Again, we can clearly see algebraic convergence of the FEM and MMP errors and the errors of the DG-based coupling are higher. However, while the convergence rate does not improve with respect to the plots of Figure 7, the values of the relative errors are much lower than before, given the easier-to-handle frequency.

4.2.1 | Minimal FEM Mesh

We repeat these experiments with the meshes shown in Figure 9, where only the points with TPS and their immediate surrounding regions are modeled with FEM, so to minimize the meshed region. Hence, here we have three MMP domains: bounded Ω_m^1, Ω_m^2 (μ_+, μ_-) and unbounded Ω_m^0 (μ_0).

To approximate in Ω_m^1 and Ω_m^2 , two multipole expansions with spherical Bessel functions as radial dependence are centered in the origin. To approximate in Ω_m^0 , a multipole expansion with spherical Hankel functions as radial dependence is also centered in the origin.

Figure 10 shows DoF-refinement convergence plots for the PDE-constrained coupling, given

- $\mu_+ = 4 \mu_0$, $\mu_- = 2.5281 \mu_0$, and $\omega = 23.56 \cdot 10^8 \text{ rad s}^{-1}$ in Figure 10a, and
- $\mu_+ = 10 \mu_0$, $\mu_- = 4 \mu_0$, and $\omega = 23.56 \cdot 10^7 \text{ rad s}^{-1}$ in Figure 10b.

We can still see algebraic convergence of the FEM and MMP errors. Moreover, the values of the relative MMP errors in Figure 10b are again much lower than Figure 10a, given the lower frequency.

We do not report results for DG-based coupling because we would have to choose 6 penalty parameters η for $\Gamma_{ij}, \Gamma_{ij}, i < j, j = 0, 1, 2$, and 3 discretization spaces $\mathcal{T}^n(\Gamma_{ij})$ to impose normal continuity between Ω_m^i, Ω_m^j (see Section 3.2).

4.2.2 | Minimal FEM Mesh and Layered Medium

We consider a similar setting to Figure 9, where the FEM mesh only surrounds the TPS, and further introduce a substrate with permeability μ_- that occupies half of \mathbb{R}^3 (with negative z -axis). Hence, the ball Ω_{\bullet} becomes a half-ball with permeability μ_+ and there is a physical discontinuity between μ_- and μ_0 on the whole XY -plane: see a sample mesh in Figure 11.

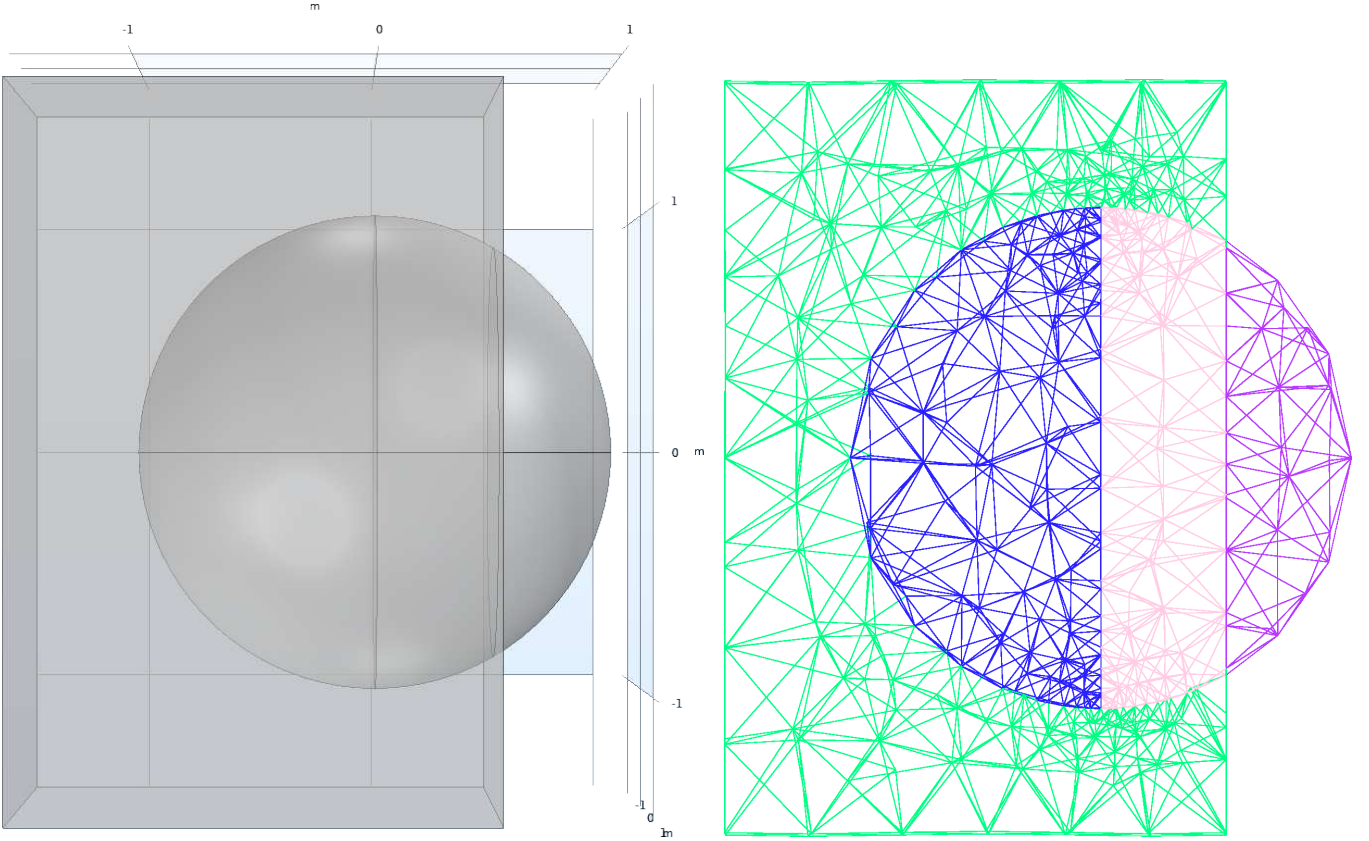


FIGURE 6 Cross-section of the 3D model (and a mesh) of Ω_f and Ω_m^1 along the XZ -plane. In the right figure, the blue, pink, and green meshes cover Ω_f and have parameters μ_+ , μ_- , and μ_0 , respectively. The purple mesh covers Ω_m^1 (μ_-) and is used for numerical quadrature of the error. For better visualization, this mesh is not locally refined at the points with TPS (circumference μ touching the blue, pink, and green meshes).

To approximate in the half-ball Ω_m^1 , multipole expansions with spherical Bessel functions as radial dependence are uniformly positioned on a rectangular prism that lies completely outside Ω_m^1 . However, to approximate in Ω_m^0 , which contains an infinite physical discontinuity,⁶ we cannot make use of the standard multipoles from Section 2.

We therefore use *layered dipoles* [?, p. 128, Section 6.3.2], which rely on the *layered-media Green's functions* reported in [?]. Their implementation includes Sommerfeld integrals, which present singularities that require integration over complex contours. Layered dipoles in Ω_m^0 are also shifted by plane waves

$$\begin{aligned}
 & \mathbf{u}_{\text{inc}} + \mathbf{u}_{\text{ref}} && \text{with } z \geq 0, \\
 & \mathbf{u}_{\text{inc}} := \exp(\imath k_0 z) (0, 1, 0)^\top, \quad \mathbf{u}_{\text{ref}} := \exp(-\imath k_0 z) (0, 1, 0)^\top A_{\text{ref}}, && (40) \\
 & \mathbf{u}_{\text{trs}} := \exp(\imath k_- z) (0, 1, 0)^\top A_{\text{trs}} && \text{with } z < 0,
 \end{aligned}$$

where $A_{\text{ref}} = \frac{\sqrt{\mu_0} - \sqrt{\mu_-}}{\sqrt{\mu_0} + \sqrt{\mu_-}}$, $A_{\text{trs}} = \frac{2\sqrt{\mu_-}}{\sqrt{\mu_0} + \sqrt{\mu_-}}$, and z_+, z_- are halves of \mathbb{R}^3 with positive/negative z -axis. (40) can be derived from standard results of reflection and transmission of plane waves with normal incidence.

Figures 12 and 13 shows DoF-refinement convergence plots for both the PDE-constrained and DG-based coupling approaches and both sets of parameters used in the previous experiments. We can see algebraic convergence of the FEM and MMP errors: in particular, the FEM convergence rates of both approaches are very similar to each other.

At the same time, plots for the higher frequency $\omega = 23.56 \cdot 10^8 \text{ rad s}^{-1}$ (Figure 12) look more irregular because of the FEM pollution effect, especially the one obtained with the DG-based coupling, where the relative errors are quite high (like in the previous experiments). With a lower frequency (Figure 13), while the relative errors of the DG-based coupling are still higher than the PDE-constrained coupling, they are at most 0.3 even for the coarsest mesh employed, and all datapoints are aligned very closely to the fitted lines.

⁶Here, Ω_m^0 does not fit into the partition of Section 1.2, where we require that $(\mu, \epsilon) \in \mathbb{C}^2$ is constant in Ω_m^0 .

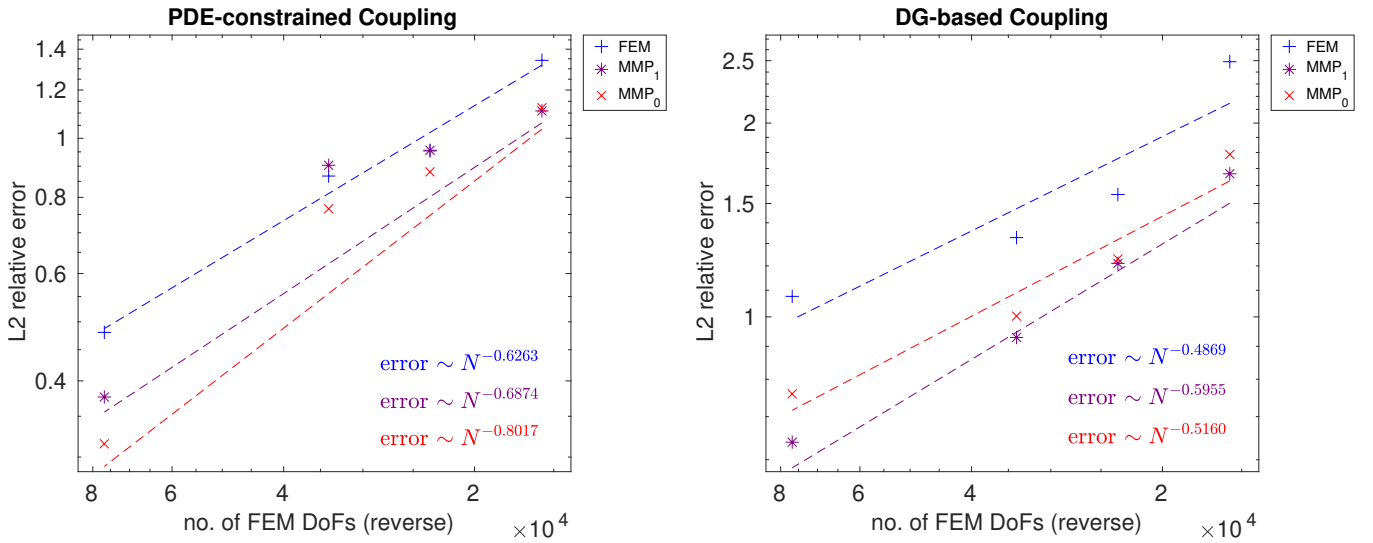


FIGURE 7 DoF-refinement log-log error plots for time-harmonic Maxwell's equations with TPS solved with two MMP domains (sample mesh in Figure 6). Parameters are $\mu_+ = 4\mu_0$, $\mu_- = 2.5281\mu_0$, and $\omega = 23.56 \cdot 10^8 \text{ rad s}^{-1}$.

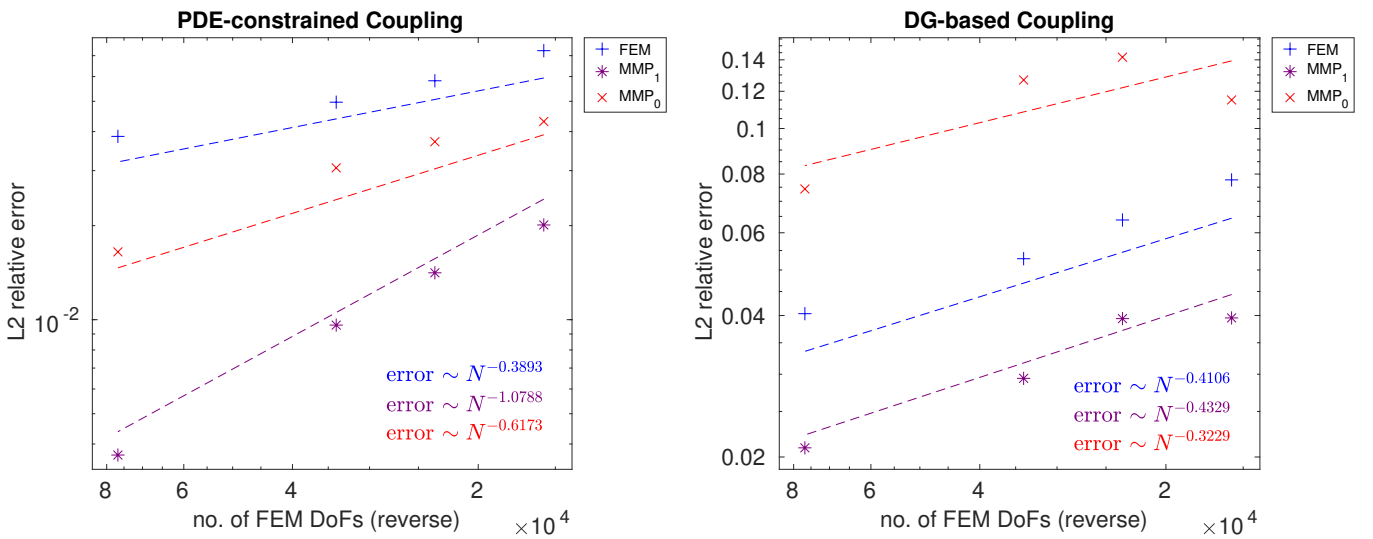


FIGURE 8 DoF-refinement log-log error plots for time-harmonic Maxwell's equations with TPS solved with two MMP domains (sample mesh in Figure 6). Parameters are $\mu_+ = 10\mu_0$, $\mu_- = 4\mu_0$, and $\omega = 23.56 \cdot 10^7 \text{ rad s}^{-1}$.

5 | CONCLUSIONS

The numerical experiments in Section 4 show the accuracy of the FEM–MMP coupling on smaller meshes than what FEM alone would require, given its artificial truncation of the computational domain. More applications of this coupling with relevance in engineering can be found in [?, p. 10, Section 4.2] (magnetostatic inductor) and [?] (conductor with a hole).

Compared to other hybrid methods, such as FEM coupled with the Boundary Element Method (BEM), MMP presents the advantages of

- a simpler assembly process, as there are no singular integrals, and
- an exponentially-convergent approximation error, given loose requirements on the positions of the multipoles (Section 2.2). As long as the coupling boundaries are far from sources and field singularities of the problem, the FEM–MMP coupling is also indifferent towards where the multipoles are placed, and the exponential convergence of the MMP approximation error is preserved.

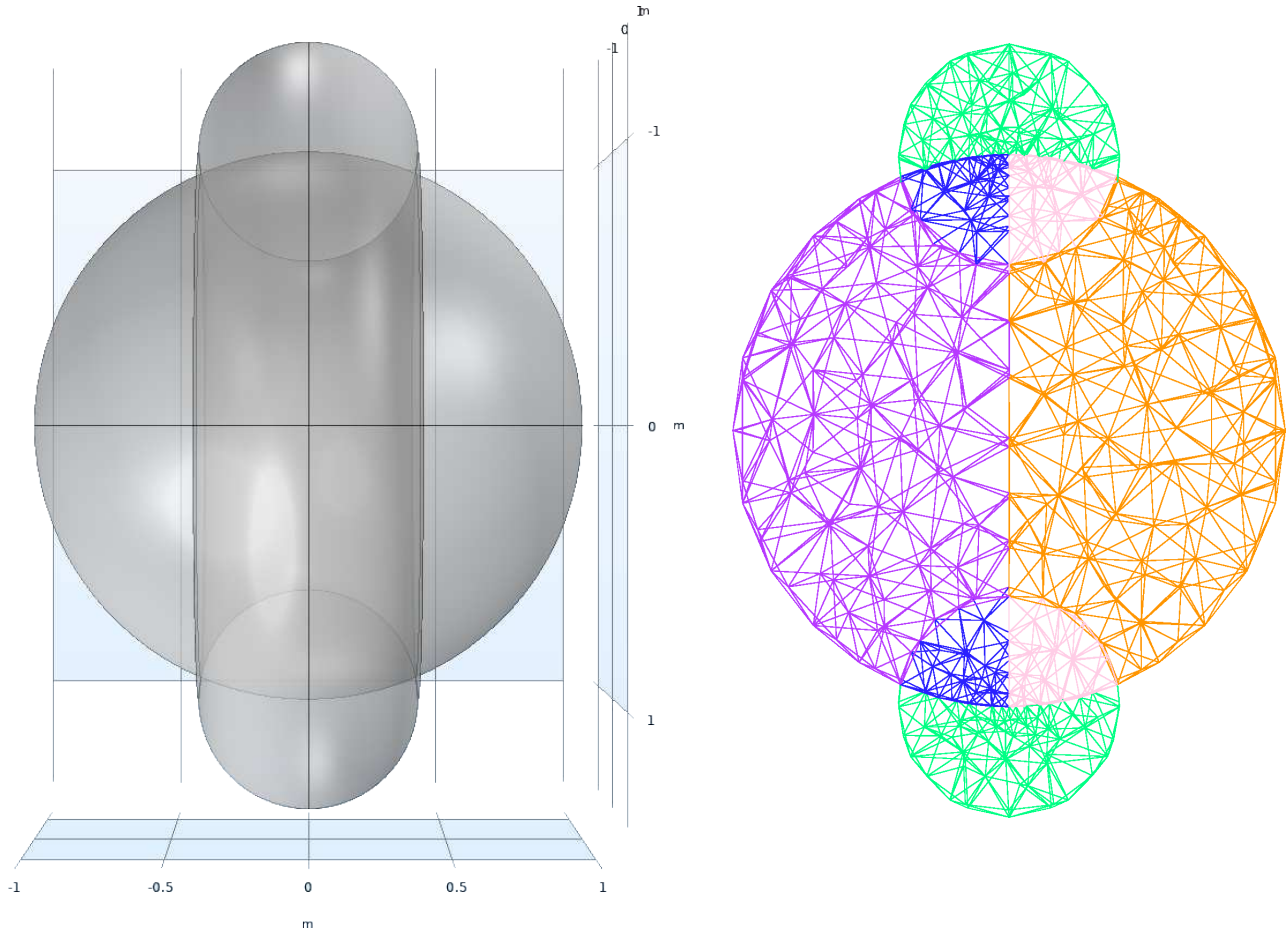


FIGURE 9 Cross-section of the 3D model (and a mesh) of Ω_f , Ω_m^1 , and Ω_m^2 along the XZ -plane. In the right figure, the blue, pink, and green meshes cover Ω_f and have parameters μ_+ , μ_- , and μ_0 , respectively. The purple and orange meshes cover Ω_m^1 (μ_+) and Ω_m^2 (μ_-). They are used for numerical quadrature of the errors.

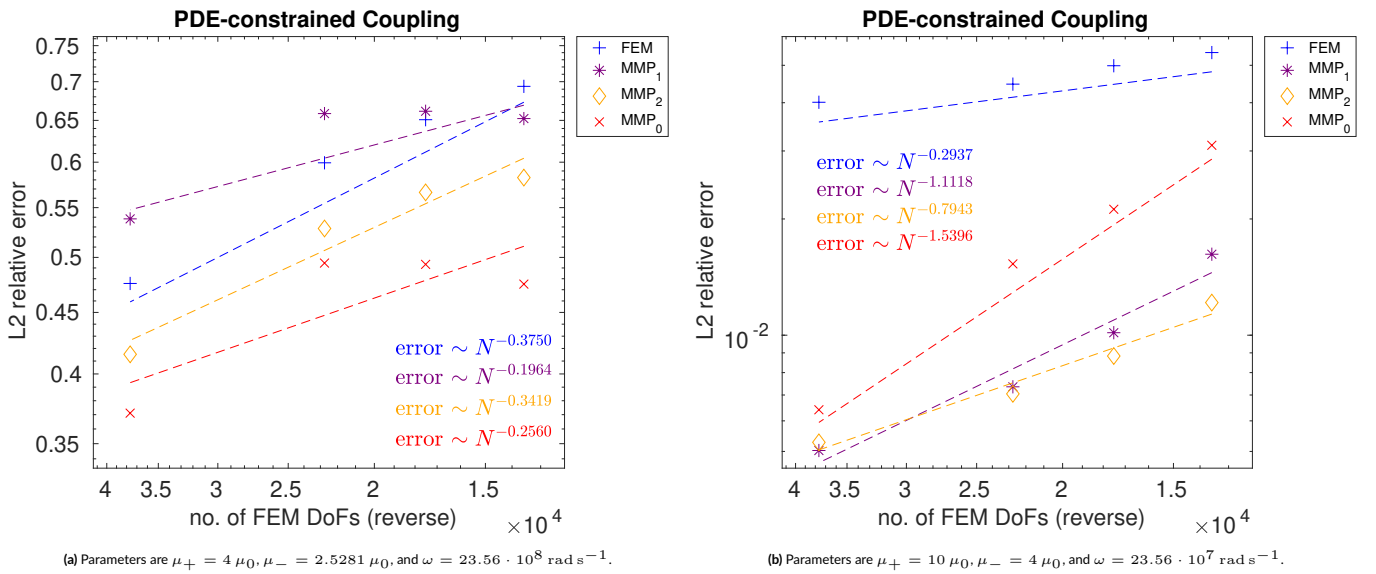


FIGURE 10 DoF-refinement log-log error plots for time-harmonic Maxwell's equations with TPS solved with three MMP domains (sample mesh in Figure 9) using the PDE-constrained coupling.

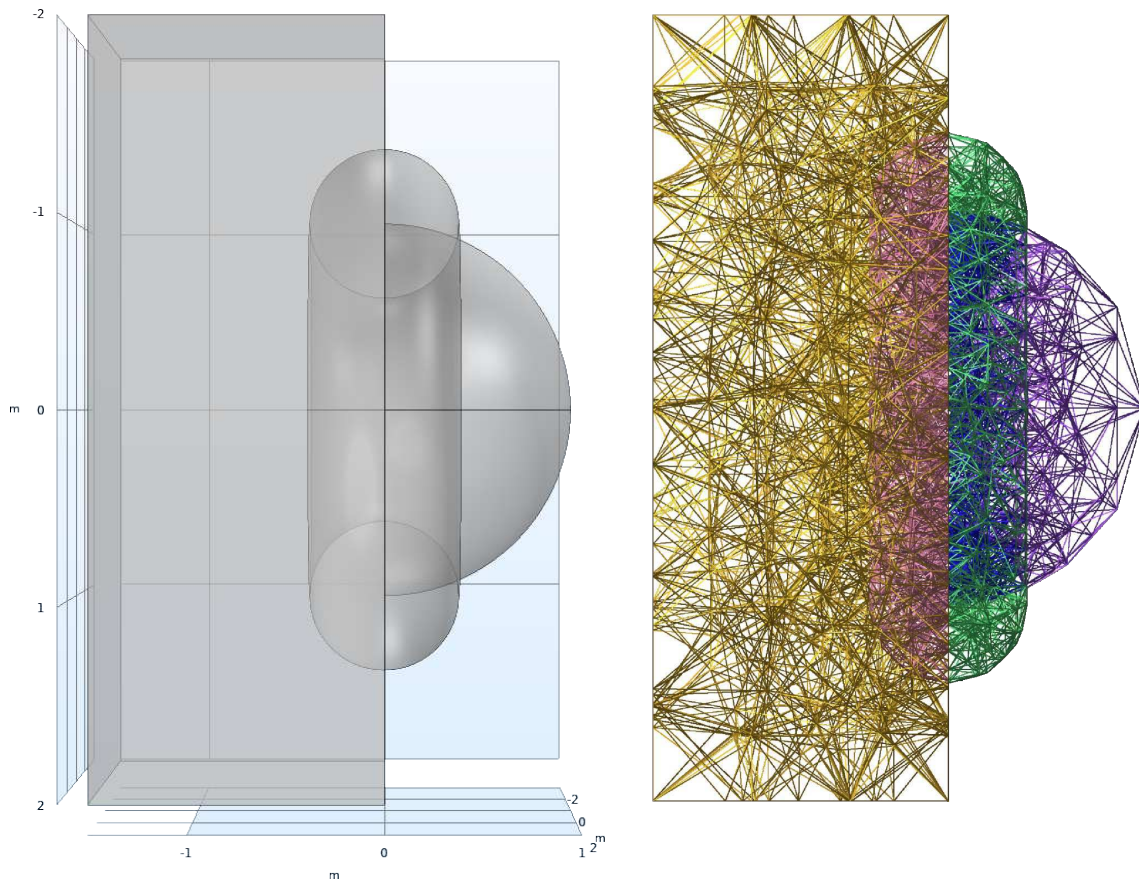


FIGURE 11 Cross-section of the 3D model (and a mesh) of Ω_f , Ω_m^1 , and a part of Ω_m^0 along the XZ -plane. In the right figure, the blue, pink, and green meshes cover Ω_f and have parameters μ_+ , μ_- , and μ_0 , respectively. The purple and orange meshes cover Ω_m^1 (μ_+) and a part of Ω_m^0 (μ_-). The mesh of Ω_m^1 is used for numerical quadrature of the error, while the mesh of Ω_m^0 only serve a graphical purpose.

- Furthermore, for high-frequency scattering problems, the locally-supported piecewise-polynomial basis functions of boundary element methods [?, p. 183, Chapter 4] may suffer from the pollution effect like FEM, which is not a problem for the oscillating multipoles.

At the same time, similarly to BEM [?], MMP also suffers from ill-conditioning. However, its impact is still more limited than BEM due to the low number of degrees of freedom required for MMP, given its exponential convergence: the dense MMP blocks in the coupling matrices are therefore small.

Between the two coupling approaches that work with multiple Trefftz domains (Sections 3.1 and 3.2), we recommend the PDE-constrained coupling thanks to its reliability, especially when the FEM mesh only surrounds field singularities. Even though this coupling requires the highest number of degrees of freedom due to its Lagrange multipliers on the FEM mesh⁷, this number is still low in absolute terms when such mesh is minimal. The DG-based coupling is less expensive, as it relies on fewer variables, but requires the additional user input of appropriate penalty parameters.

Conversely, among all coupling strategies, methods based on the tangential components trace stand out (Sections 3.3.1 and 3.3.2): both the multi-field and DtN-based approaches combine a sensibly lower number of degrees of freedom than the PDE-constrained coupling without the penalty parameters of the DG-based one. In particular, the DtN-based coupling is the easiest to implement: MMP degrees of freedom can even be eliminated by a Schur complement approach, paving the way for an iterative solver [?].

⁷Hence, the PDE-constrained coupling doubles the number of FEM degrees of freedom. Conversely, the number of degrees of freedom of all the other coupling approaches is approximately the same as standard FEM. Indeed, the other degrees of freedom, coming from MMP or other Lagrange multipliers, are comparatively a negligible quantity: the former because of the exponential convergence of MMP, the latter because those degrees of freedom are linked to MMP itself or the FEM discretization restricted to the mesh boundary.

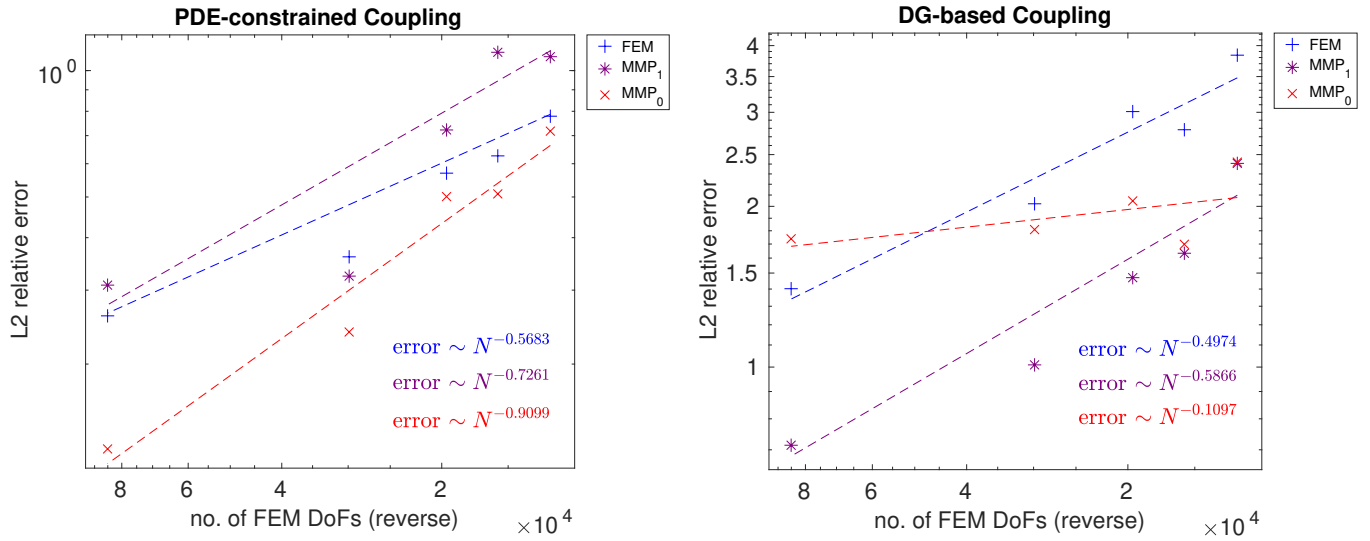


FIGURE 12 DoF-refinement log-log error plots for time-harmonic Maxwell's equations with TPS solved with two MMP domains (sample mesh in Figure 11) and layered dipoles. Parameters are $\mu_+ = 4\mu_0$, $\mu_- = 2.5281\mu_0$, and $\omega = 23.56 \cdot 10^8 \text{ rad s}^{-1}$.

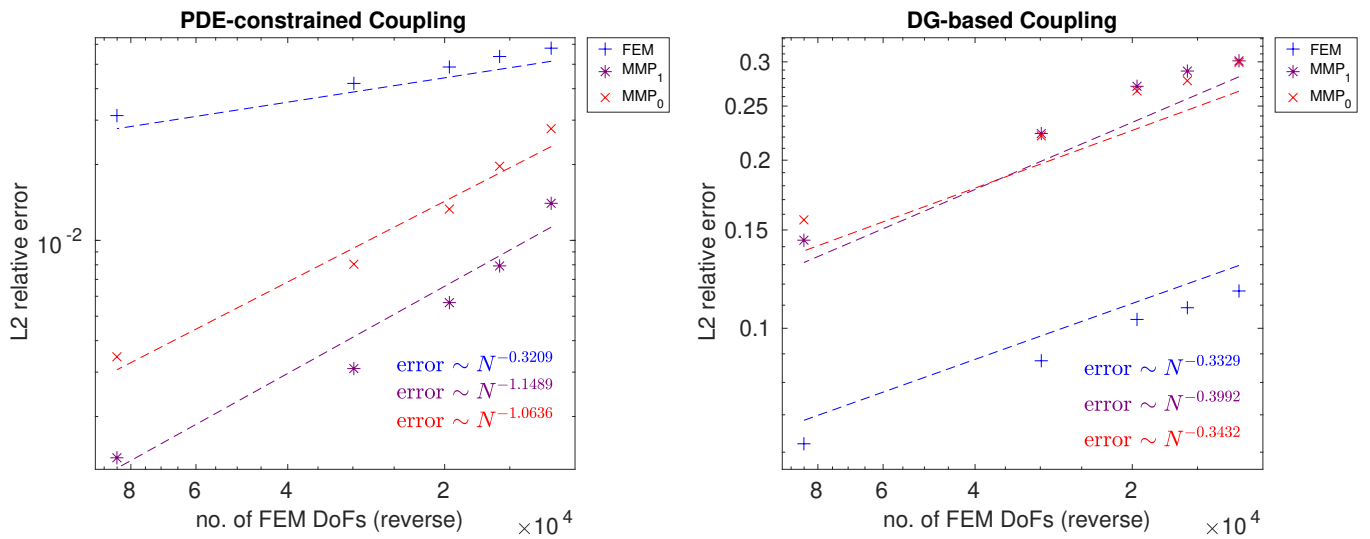


FIGURE 13 DoF-refinement log-log error plots for time-harmonic Maxwell's equations with TPS solved with two MMP domains (sample mesh in Figure 11) and layered dipoles. Parameters are $\mu_+ = 10\mu_0$, $\mu_- = 4\mu_0$, and $\omega = 23.56 \cdot 10^7 \text{ rad s}^{-1}$.

ACKNOWLEDGMENTS

This work was supported by the Swiss National Science Foundation [grant number 2000021_165674/1].

The FEM component of our implementation relies on `HyDi`, a C++14 library that was written during the PhD project of R. Casagrande at ETH Zurich [?] in collaboration with Ch. Winkelmann (ABB Corporate Research Center): we gratefully acknowledge their contribution.

We also acknowledge U. Koch, researcher at the Institute of Electromagnetic Fields of ETH Zurich (D-ITET), for his C++ implementation of layered dipoles [?, p. 128, Section 6.3.2].

